Journal of Nanobiotechnology

RESEARCH

Open Access

# A ROS-responsive hydrogel encapsulated with matrix metalloproteinase-13 siRNA nanocarriers to attenuate osteoarthritis progression

Qiuyang Wang[1,2,3†], Kai Feng[4†], Guangsheng Wan[4†], Wei Liao[5], Jing Jin[1], Peng Wang[1,2,3*], Xiaolian Sun[4*], Weijun Wang[1,2,3*] and Qing Jiang[1,2,3*]

## Abstract

RNA interference (RNAi) and oxidative stress inhibition therapeutic strategies have been extensively utilized in the treatment of osteoarthritis (OA), the most prevalent degenerative joint disease. However, the synergistic effects of these approaches on attenuating OA progression remain largely unexplored. In this study, matrix metalloproteinase-13 siRNA (siMMP-13) was incorporated onto polyethylenimine (PEI)-polyethylene glycol (PEG) modified $Fe_3O_4$ nanoparticles, forming a nucleic acid nanocarrier termed si-Fe NPs. Subsequently, a poly(vinyl alcohol) (PVA) crosslinked phenylboronic acid (PBA)-modified hyaluronic acid (HA) hydrogel (HPP) was used to encapsulate the si-Fe NPs, resulting in a bifunctional hydrogel (si-Fe-HPP) with reactive oxygen species (ROS)-responsive and RNAi therapeutic properties. Studies *in vitro* demonstrated that si-Fe-HPP exhibited excellent biocompatibility, anti-inflammatory effects and prolonged stable retention time in knee joint. Intra-articular injection of si-Fe-HPP significantly attenuated cartilage degradation in mice with destabilization of the medial meniscus (DMM)-induced OA. The si-Fe-HPP treatment not only notably alleviated synovitis, osteophyte formation and subchondral bone sclerosis, but also markedly improved physical activity and reduced pain in DMM-induced OA mice. This study reveals that si-Fe-HPP, with its ROS-responsive and RNAi abilities, can significantly protect chondrocytes and attenuate OA progression, providing novel insights and directions for the development of therapeutic materials for OA treatment.

**Keywords** Osteoarthritis, Metalloproteinase-13 siRNA nanocarrier, ROS-responsive Hydrogel

†Qiuyang Wang, Kai Feng and Guangsheng Wan have contributed equally to this work as the first authors.

*Correspondence:
Peng Wang
15850681759@163.com
Xiaolian Sun
xiaolian_sun@cpu.edu.cn
Weijun Wang
drwilliamwang@163.com
Qing Jiang
qingj@nju.edu.cn
Full list of author information is available at the end of the article

**Graphical Abstract**

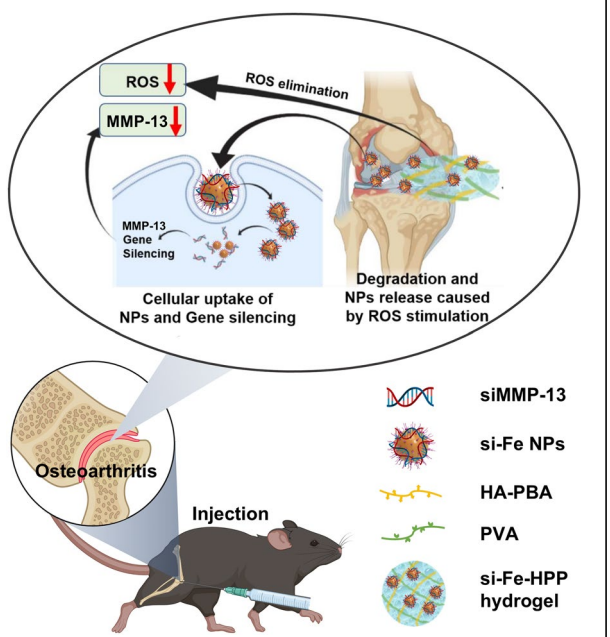


## Introduction

Osteoarthritis (OA) is one of the leading causes of disability in the elderly and is the most prevalent joint disease, characterized by the degradation of cartilage extracellular matrix (ECM), subchondral bone sclerosis, and synovitis [1–3]. Although the pathogenesis of OA is complex, primary investigations have indicated that oxidative stress-mediated articular cartilage degradation is a major pathological process [4]. Consequently, as osteoarthritis progresses, patients experience chronic joint pain, reduced mobility, and a diminished quality of life [5]. Currently, most clinical treatments for OA rely on non-steroidal anti-inflammatory drugs (NSAIDs) or surgical interventions, such as arthroplasty [6]. However, long-term use of anti-inflammatory drugs can lead to serious side effects, including gastrointestinal ulcers and perforation [7]. Therefore, it is imperative to develop highly effective and potent therapies to protect articular cartilage from degradation and to mitigate oxidative stress during the progression of OA.

Currently, there are several factors, including inflammatory cytokines, aggrecanases (ADAMTS) and matrix metalloproteinases (MMPs), that play significant roles in the occurrence and progression of OA [8]. Inflammatory cytokines, such as interleukin-1β (IL-1β), tumor necrosis factor-α (TNF-α), can also drive the catabolic processes in OA by stimulating the production of MMPs [9, 10]. Several MMPs, particularly MMP-1, MMP-3, and MMP-13, are heavily involved in the breakdown of cartilage collagen (specifically type II collagen) and proteoglycans, contributing to the structural degradation of the joint [11]. Among them, MMP-13 is considered as one of the most critical enzymes in the degradation of type II collagen, the major structural protein in articular cartilage [12]. MMP-13 is highly upregulated in OA and plays a central role in cartilage destruction, making it a compelling target for therapeutic intervention [13]. However, there is no effective therapeutic regimen that directly targets MMP-13 [12, 14]. Over the past decade, gene therapy based on the delivery of small interfering RNA (siRNA) has emerged as an effective treatment for a variety of diseases including OA [15], neurological disorders [16, 17], and liver-associated disorders [18]. RNA interference (RNAi) is a biological process in which small RNA molecules, such as siRNA, induce the degradation of specific messenger RNA (mRNA) molecules, thereby silencing the expression of target genes [19]. In therapeutic applications, synthetic siRNA molecules are designed to match the sequence of a disease-related gene [20]. Upon delivery into cells, the siRNA is incorporated into the RNA-induced silencing complex (RISC), which recognizes and cleaves the complementary mRNA, effectively reducing the production of the target protein [21]. This precise gene-silencing mechanism makes RNAi a promising approach for diseases where specific gene overexpression contributes to pathogenesis [22]. Thus, the application of intra-articular injection to deliver therapeutic siRNAs holds great potential for the treatment of OA [13, 23]. While RNAi holds great potential as a therapeutic approach, delivering naked siRNA (unprotected siRNA molecules) faces significant challenges [24]. Naked siRNA is rapidly degraded by nucleases in biological environments, exhibits poor cellular uptake, and is cleared quickly from circulation [25]. These limitations significantly reduce the therapeutic efficacy of siRNA when administered alone. Fortunately, nanomedicine, an emerging multidisciplinary field, has demonstrated a promising ability to overcome the therapeutic limitations of siRNAs [13]. Various nano-carriers, including polymeric micelles, organosilicons, iron oxides, and gold nanoparticles, have been employed to deliver siRNAs, DNAs, plasmids, or oligonucleotides to cells, enhancing drug stability and increasing cellular uptake [26–28]. $Fe_3O_4$ nanoparticles ($Fe_3O_4$ NPs) are well-documented for their biocompatibility and ease of functionalization, making them suitable candidates for various biomedical applications [29]. One advantage of $Fe_3O_4$ NPs is its universality for surface modification of functional molecules, such as polyethyleneimine (PEI), Bovine serum albumin (BSA) to achieve various biological applications. Among them, PEI, a cationic polymer, facilitates the efficient binding

of negatively charged siRNA through electrostatic interactions, significantly enhancing the loading capacity and cellular uptake of siRNA [30]. Although PEI is known for its high transfection efficiency, it is also associated with cytotoxicity due to its strong positive charge [31]. To reduce the cytotoxicity of PEI, significant efforts have focused on functionalizing nanoparticles with polyethylene glycol (PEG), a widely used strategy to enhance biocompatibility by lowering surface charge and masking PEI's cationic properties [32]. This PEGylation strategy reduces the cytotoxicity of PEI while preserving its siRNA delivery capabilities [30, 33]. Therefore, the development of siRNA nanomaterial delivery methods offers a new opportunity to directly target MMP-13 and inhibit cartilage degeneration.

To complement RNAi-mediated targeting of cartilage degradation, an additional strategy focuses on mitigating oxidative stress, both of which are essential for slowing OA progression. Previous studies have identified oxidative stress as a significant promoter of the development and progression of OA [4, 34]. Specifically, oxidative stress can further induce chondrocyte apoptosis, upregulate MMP-13 expression, and inhibit autophagic processes [35, 36]. Thus, reducing reactive oxygen species (ROS) in the local microenvironment of OA is crucial for delaying disease progression [37–39]. A dual approach that both improves the oxidative stress microenvironment and targets ROS-mediated MMP-13 upregulation in chondrocytes could provide a synergistic therapeutic strategy to slow OA progression. However, most current antioxidant drugs are small molecules that are easily cleared from the body, resulting in unstable effects [38]. Therefore, it is essential to explore long-acting, stable, and effective methods to combat oxidative stress. Recently, hydrogels are crosslinked networks of hydrophilic polymers, which can be derived from either natural or synthetic polymers [40, 41]. Currently, polymers such as hyaluronic acid (HA), chondroitin sulfate (CS), and collagen have been developed into hydrogels with anti-inflammatory and cartilage-repairing properties [42]. These hydrogels exhibit excellent biocompatibility as they are natural polysaccharides inherent in the extracellular matrix of cartilage [43]. Given these advantages, there has been a surge in research exploring the use of these hydrogel materials for the treatment of OA. Hydrogels can be broadly classified into two main categories: non-responsive and responsive types. Non-responsive hydrogels retain their inherent properties irrespective of environmental changes. In contrast, responsive hydrogels undergo notable physical or chemical transformations in response to specific stimuli, including variations in pH, light, temperature, magnetic fields, or the presence of biomolecules [44, 45]. The inability of non-responsive hydrogels to adapt to the severity of OA restricts their therapeutic flexibility and efficacy [46]. In contrast, hydrogels engineered to respond to elevated ROS levels can actively scavenge ROS and degrade on-demand, releasing encapsulated therapeutic agents when oxidative stress within the joint triggers their response. Thus, a responsive hydrogel system with dual therapeutic action offers both sustained release of siRNA targeting MMP-13 and mitigation of ROS, addressing both cartilage degradation and oxidative stress associated with OA progression.

In this study, we designed and synthesized cationic small-size nanoparticles ($Fe_3O_4$-PEI-PEG NPs) and efficiently loaded MMP-13 siRNA (siMMP-13) onto these nanoparticles to form nucleic acid-nanoparticle complexes (si-Fe NPs). These complexes facilitate the intracellular delivery of siMMP-13 and protect siRNA from degradation, thereby enhancing the silencing effect of siMMP-13. Subsequently, si-Fe NPs were incorporated into an injectable hydrogel (HPP hydrogel) capable of scavenging $H_2O_2$. This hydrogel was formed by crosslinking phenylboronic acid (PBA)-modified HA with polyvinyl alcohol (PVA) through borate bond formation, resulting in a nanocomposite hydrogel for the encapsulation of si-Fe NPs. The resulting nanocomposite hydrogel (si-Fe-HPP) synergizes the therapeutic effects of MMP-13 gene silencing and ROS scavenging to suppress joint inflammation and promote cartilage repair. Moreover, the si-Fe-HPP hydrogel responds to elevated $H_2O_2$ levels (50–100 μM) in the inflammatory environment. High concentrations of $H_2O_2$ accelerate the release of si-Fe NPs when inflammation is aggravated, while the hydrogel prolongs the retention of si-Fe NPs when inflammation is alleviated. This responsive behavior enables the construction of an intelligent, slow, and controlled drug delivery system for various kinds of biomedical applications (Fig. 1).

## Results and discussion

### Preparation, characterization, and biological properties of $Fe_3O_4$-PEI-PEG NPs and si-Fe NPs

To evaluate the efficacy of three siRNA sequences (Table S1) in suppressing MMP-13 expression, C28/I2 cells pretreated with transfection reagent were exposed to 80 pmol/mL siRNAs (siMMP-13–1062, siMMP-13–1270, and siMMP-13–1335, all synthesized by Shanghai GenePharma Co., Ltd.). After 4–6 h of incubation, Real-time quantitative polymerase chain reaction (RT-qPCR) analysis was performed to assess gene expression levels. And the results demonstrated that both siMMP-13–1270 and siMMP-13–1335 significantly reduced MMP-13 expression with satisfactory silencing effects (Fig. S1). In our study, we selected the siRNA sequence

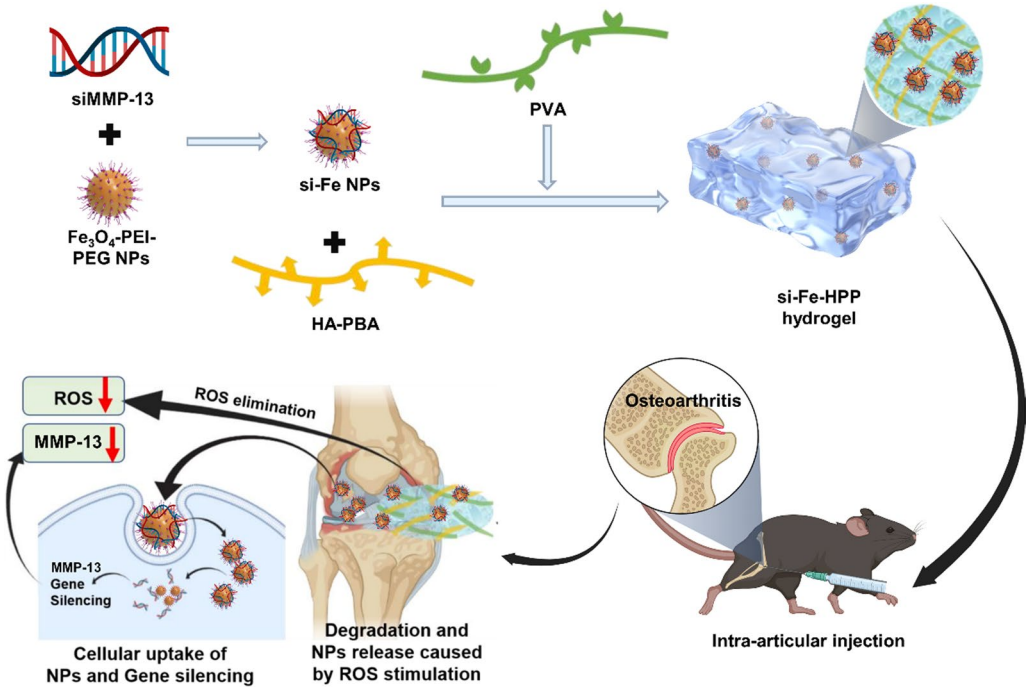


**Fig. 1** Schematic diagram of preparation process and action mechanism of si-Fe-HPP hydrogel to attenuate osteoarthritis progression

siMMP-13–1335 for further investigations. We initially synthesized oleylamine-coated $Fe_3O_4$ nanoparticles (NPs) [47], and transmission electron microscopy (TEM) results (Fig. S2) confirmed the successful synthesis of uniformly sized $Fe_3O_4$ NPs with good dispersion, and particle sizes ranged from 10 to 20 nm. To enhance the adsorption of siMMP13 via electrostatic interactions, we functionalized the $Fe_3O_4$ surfaces with the cationic polymer PEI-PEG, the process of which is schematically shown in Fig. 2a. The nuclear magnetic resonance ($^1$H NMR) spectrum of PEI-PEG (Fig. S3) revealed that all major hydrogen atoms were present as corresponding peaks, indicating their successful synthesis. After surface modification of PEI-PEG, the morphology of $Fe_3O_4$-PEI-PEG NPs did not alter compared with neat $Fe_3O_4$ (Fig. 2b). Moreover, nucleic acid-nanoparticle complex (si-Fe NPs) were obtained by mixing siRNA with $Fe_3O_4$-PEI-PEG NPs through electrostatic adsorption. Slight increase of particle aggregation could be observed after siRNA adsorption, which could be attributed to the incomplete modification of surface charges (Fig. 2c) [48]. $Fe_3O_4$-PEI-PEG NPs exhibited an average hydrodynamic size of approximately 47 nm. Upon loading with siRNA at a siRNA mass ratio of 16:1 (siRNA: Fe), there was a significant increase in the hydrodynamic size of si-Fe NPs to approximately 116 nm, while maintaining good dispersion (Fig. 2d). Zeta potential, indicative of the surface charge potential of particles in solution, was evaluated for si-Fe NPs with varying siRNA mass ratios (Fig. 2e). Initially, pure $Fe_3O_4$-PEI-PEG NPs exhibited a surface potential of +33 mV, owing to the positively charged PEI-PEG polymer ligand, facilitating the adsorption of negatively charged nucleic acids. As the mass ratio of siRNA increased, the positive surface charge gradually neutralized due to nucleic acid binding, resulting in a decrease in the surface potential of si-Fe NPs. At a siRNA mass ratio of 24:1, the surface charge reached −1.1 V, indicating that the positive charge of the system had been neutralized by the negative charge, resulting in negatively charged NPs. Gel electrophoresis results suggested that at siRNA mass ratios ≥24:1, the NPs became negatively charged, and some free siRNA was present, meaning the siRNA was not fully protected (Fig. 2f). This behavior was consistent with Zeta potential measurements, confirming that NPs were negatively charged at siRNA ratios ≥24:1. When siRNA was loaded onto $Fe_3O_4$-PEI-PEG NPs at a 16:1 ratio, the Zeta potential reached approximately +6.9 mV, which could promote efficient cellular transfection of the siRNA-loaded NPs while reducing the cytotoxicity typically associated with cationic nanocomplexes. This favorable charge profile establishes a strong foundation for nanoparticle entry into cells, enabling effective gene silencing. Hence, si-Fe NPs with a siRNA ratio of 16:1, were selected for subsequent experiments. Quantitative analysis of Fe concentration in the composites modified with PEI-PEG was performed to determine

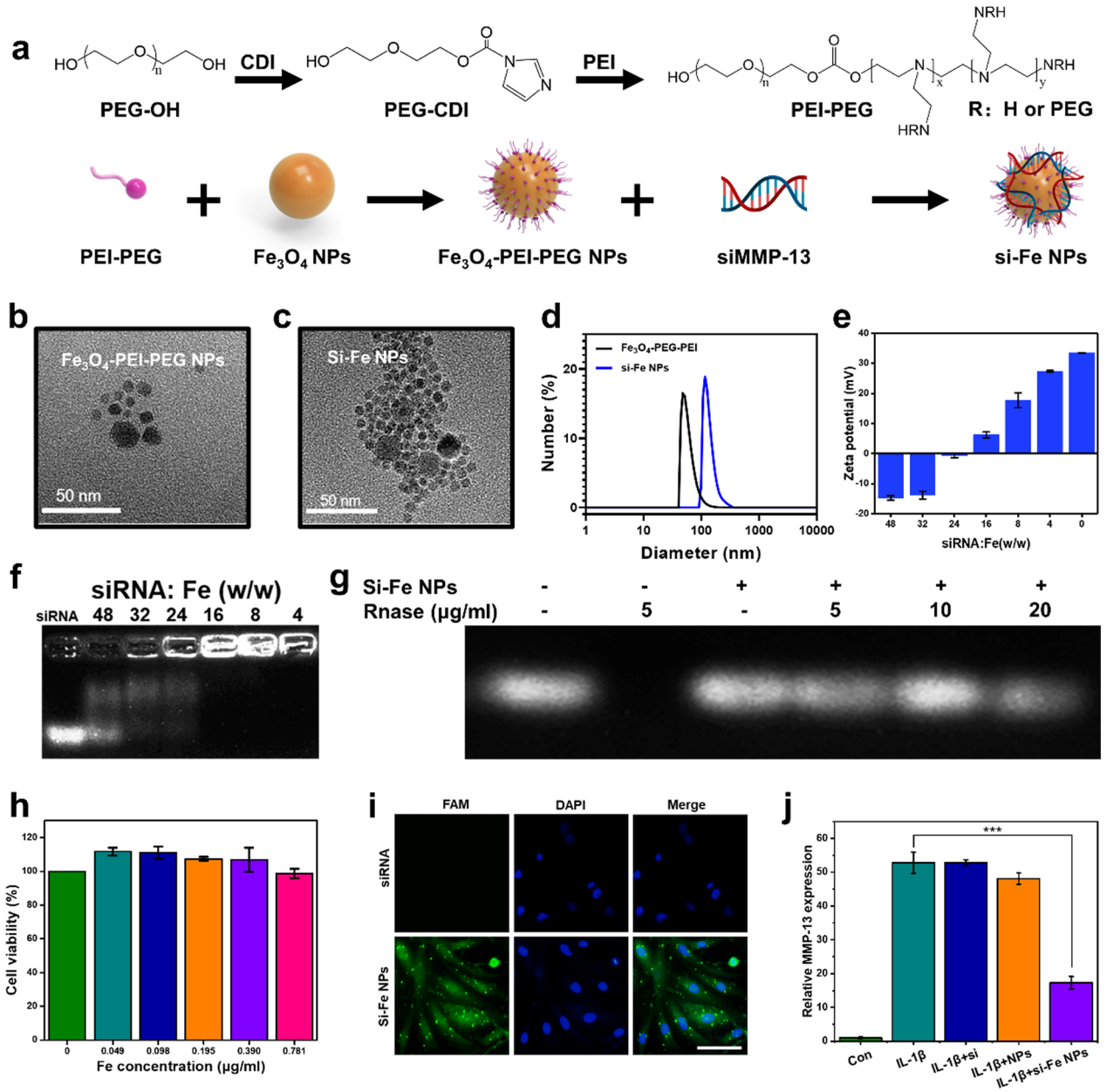


**Fig. 2** Preparation, characterization, and biological properties of $Fe_3O_4$-PEI-PEG NPs and si-Fe NPs. **a** Schematic diagram of preparation of $Fe_3O_4$-PEI-PEG NPs and si-Fe NPs. **b**–**c** TEM image of **b** $Fe_3O_4$-PEI-PEG NPs and **c** si-Fe NPs. Scale bar: 50 μm. **d** The average hydrodynamic particle size distribution of $Fe_3O_4$-PEI-PEG NPs and si-Fe NPs. **e** Zeta potentials of si-Fe NPs at various weight ratios of siRNA:Fe. **f** Agarose gel retardation assay of si-Fe NPs at various weight ratios of siRNA:Fe. **g** The protective effect of $Fe_3O_4$-PEI-PEG NPs on siRNA against RNase digestion. **h** Cell viabilities of C28/I2 cell line detected by MTT with various concentrations of si-Fe NPs. **i** Fluorescence image of C28/I2 cell line incubated with naked FAM-siRNA or FAM si-Fe NPs for 12 h. scale bar: 50 μm. **j** MMP-13 gene silencing efficacy of si-Fe NPs on C28/I2 cell line

Fe content. Iron concentration-absorbance standard curves (Fig. S4) exhibited good linearity over the range of 0–10 μg/mL iron standard solutions. Subsequently, we assessed the ability of si-Fe NPs to protect siRNAs against degradation. As depicted in Fig. 2g, si-Fe NPs demonstrated substantial fluorescence intensity even in the presence of 20 μg/mL RNase, indicating effective protection of loaded siRNA by $Fe_3O_4$-PEI-PEG NPs under complex biological conditions. Biocompatibility evaluation is essential for biomedical materials. Therefore, we conducted MTT assays to assess cytocompatibility of si-Fe NPs at various concentrations (Fig. 2h). Results

indicated that concentrations up to 0.781 μg/mL Fe did not adversely affect chondrocyte viability, underscoring the biocompatibility of si-Fe NPs for potential therapeutic applications. Additionally, cellular uptake capacity of si-Fe NPs was evaluated. For the si-Fe NPs group, FAM-siNC-Fe NPs were formulated, while the free siRNA group received equivalent amounts of free FAM-siNC. As shown in Fig. 2i, free siRNAs failed to enter chondrocytes, whereas si-Fe NPs exhibited significant green fluorescence within chondrocytes, demonstrating the ability of $Fe_3O_4$-PEI-PEG NPs to deliver siRNA effectively. Finally, we assessed the MMP-13 gene silencing efficacy of si-Fe NPs in C28/I2 cell lines. IL-1β stimulation significantly upregulated MMP-13 gene expression in chondrocytes (Fig. 2j). Free siMMP-13 compared with negative control nano-composites loaded with siRNA (Negative Control) (siNC) did not effectively suppress MMP-13 expression (Table S1), likely due to instability of naked siMMP-13. Moreover, $Fe_3O_4$-PEI-PEG NPs alone did not exhibit MMP-13 inhibitory effects (Fig. 2j). In contrast, si-Fe NPs significantly reduced IL-1β-induced MMP-13 expression, demonstrating superior MMP-13 gene silencing efficacy and stability compared to free siRNA (Fig. 2j). Hence, the encapsulation of siMMP-13 with $Fe_3O_4$-PEI-PEG NPs overcomes the instability issues associated with naked siMMP-13, facilitating enhanced cellular uptake and sustained therapeutic efficacy. Moreover, excellent biocompatibility of si-Fe NPs supports their further development for biomedical applications.

### Preparation, characterization and biological properties of HPP hydrogel

A schematic diagram illustrating the fabrication of the HPP hydrogel is presented in Fig. 3a. Initially, HA was modified with phenylboronic acid (PBA), as depicted in the synthesis route (Fig. S5). The presence of characteristic peaks of hydrogen atoms on the benzene ring of PBA in Fig. S6 confirmed the successful attachment of PBA to the HA backbone, with a calculated grafting rate of approximately 47.2%. The PVA solution was added to the HA-PBA solution and mixed while stirring to ensure uniform blending. After 5–10 s of stirring, the mixture condensed into a viscous solid in the EP tube. To eliminate air bubbles, the mixture was centrifuged at 10,000 rpm. Successful gelation of the HPP hydrogel was confirmed by inverting the EP tube, with no liquid flow indicating proper formation [49]. To evaluate the hydrogel formation, we used a 2% + 9% HPP hydrogel as a representative example. As shown in Fig. 3b, fluorescent molecules Cy5 and Rhodamine B were mixed into 180 μL of HA-PBA and 60 μL of PVA solutions, resulting in dark green and red solutions, respectively. The resultant gelatinous solid adhered to the bottom of the tube, with no liquid flow observed, indicating successful hydrogel formation. Scanning electron microscopy (SEM) images (Fig. 3c) revealed that the HPP hydrogels were tightly crosslinked with numerous internal pores. Rheological properties of the HPP hydrogel were characterized through strain scan, frequency scan, time scan, and recovery scan, as shown in Fig. 3d–f and Fig. S7. Figure 3d illustrates that the HPP hydrogel remains in a solid state under strains less than 190%, transitioning to a liquid state at higher strains, a phenomenon known as shear thinning, supporting the hydrogel's injectability. In the frequency scan (Fig. 3e), both the storage modulus ($G'$) and loss modulus ($G''$) of the HPP hydrogel increased significantly between 0.1 to 20 Hz. At 1% strain and 1 Hz angular velocity, $G'$ reached approximately 4200 Pa and $G''$ approximately 2000 Pa (Fig. 3f), indicating that the hydrogel maintained its solid state and stability over time. The step strain test (Fig. S7) showed that under 1% strain, $G' > G''$, indicating a stable solid state. At 1000% strain, the internal network of the hydrogel was disrupted, with $G' < G''$, resulting in a liquid state. The PBA molecules recombined with the diol structure on PVA, forming borate bonds, which reverted the hydrogel to its original solid state. This transient and dynamically bonded nature of the borate bond imparts self-healing and injectable properties to the hydrogel. Given the slow process of OA repair, hydrogel materials must exhibit prolonged retention within the joint. To assess long-term retention and ROS responsiveness in both normal and inflamed joints, phosphate-buffered saline (PBS) and 100 μM $H_2O_2$ were used to simulate physiological conditions. Figure S8 demonstrates the degradation profiles of nine different hydrogel formulations in PBS or $H_2O_2$. The 2% + 9% HPP hydrogel exhibited

(See figure on next page.)

**Fig. 3** Preparation, characterization, and biological properties of HPP hydrogel. **a** Schematic diagram of preparation of HPP hydrogel. **b** The formation process of HPP hydrogel. **c** SEM image of HPP hydrogel. Scale bar: 200 μm. **d**–**f** Rheological characterization of HPP hydrogel. **d** Strain sweep test; **e** Frequency sweep test; **f** Time sweep test. **g** Degradation of HPP hydrogel in PBS and different concentrations of $H_2O_2$. **h** UV–vis spectroscopy of NaI/$H_2O_2$ solution with or without HPP hydrogel co-incubation. **i**–**j** Cell viabilities of C28/I2 cell line detected by MTT assays **i** with various concentrations of HPP hydrogel and **j** with various concentrations of $H_2O_2$ with or without HPP Hydrogel. **k**–**l** Cell viabilities (**k**) of C28/I2 cell line detected by Live/Dead staining at 1 mM $H_2O_2$ with or without HPP Hydrogel, followed by quantitative analysis of the results (**l**). Scale bar: 200 μm. **m** Residence time of the HPP hydrogel in knee joint of normal and model mice

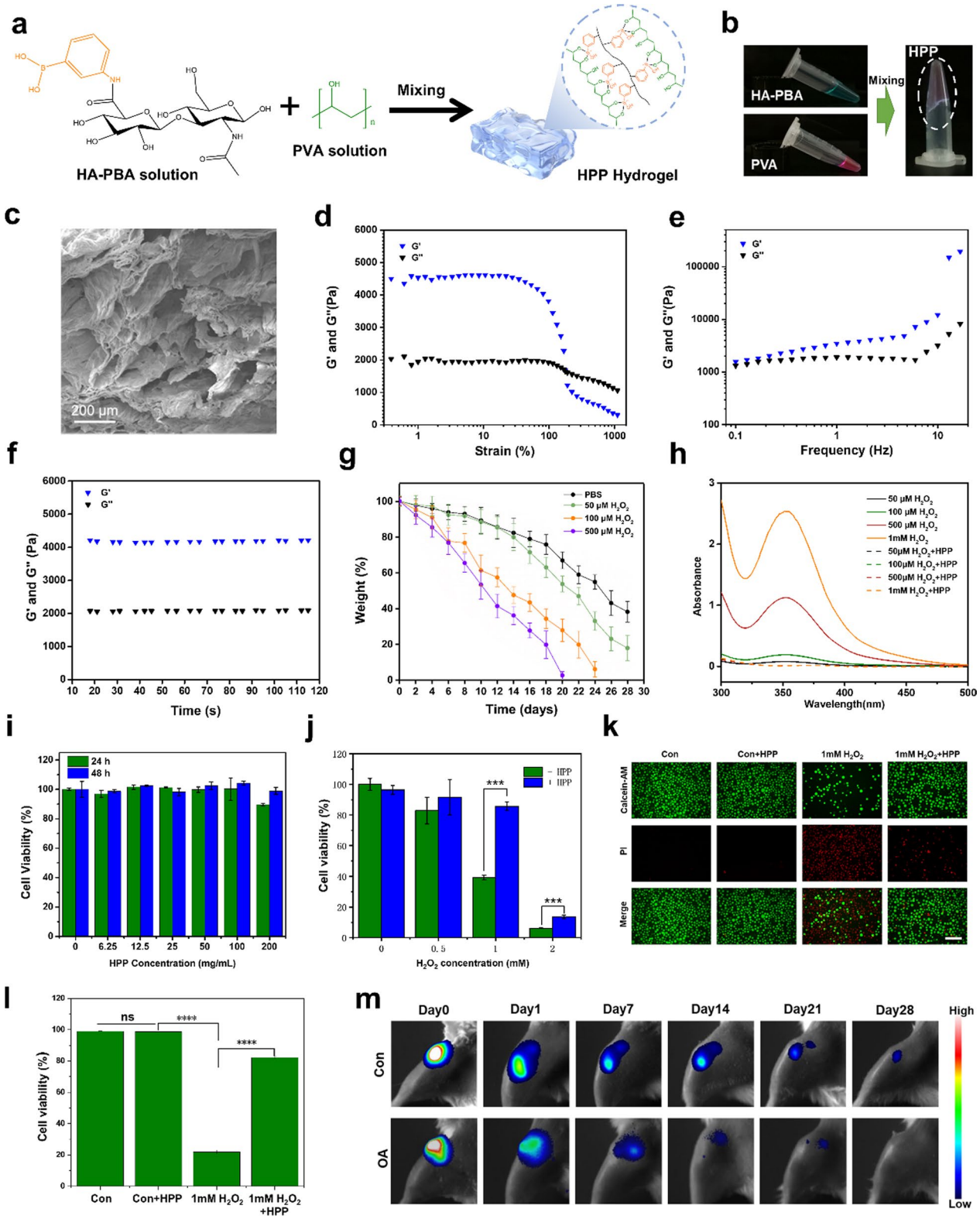


**Fig. 3** (See legend on previous page.)

both long-term stability and ROS responsiveness, making it suitable for subsequent in vitro and in vivo experiments. Then, the ROS-responsive degradation behavior of HPP hydrogels was systematically examined. A significant reduction in the mass of the HPP hydrogel was observed in different concentrations of $H_2O_2$ solution, indicating a characteristic ROS-responsive degradation (Fig. 3g). Specifically, $H_2O_2$ (100 μM) present at arthritic sites could induce hydrogel degradation, thereby facilitating the intelligent and controlled release of therapeutic agents at the OA site. Furthermore, we validated the in vitro $H_2O_2$ scavenging ability of the HPP hydrogel. NaI oxidation by $H_2O_2$ results in an oxidation product with an absorption peak at 350 nm, allowing the determination of $H_2O_2$ content in the system. As shown in Fig. 3h, 100 μL of hydrogel could completely remove 500 μL of 1 mM $H_2O_2$ within a short period, indicating the high $H_2O_2$ removal efficiency of the HPP hydrogel. This property has the potential to alleviate oxidative stress in the joint area, inhibit the progression of inflammation, and benefit the treatment of OA.

The biocompatibility of HPP hydrogels was evaluated, demonstrating non-toxicity to chondrocytes within a concentration range of 0–200 mg/mL, with cell survival rates consistently above 80% and predominantly near 100% (Fig. 3i). This favorable biocompatibility underpins subsequent cellular and animal experiments. Chondrocyte activity following various treatments was analyzed using the MTT assay and live/dead cell staining. Increased $H_2O_2$ concentrations significantly elevated cell death rates, with survival dropping below 40% at 1 mM $H_2O_2$. However, the presence of HPP hydrogel notably enhanced cell survival compared to the $H_2O_2$ group alone (Fig. 3j). Live/Dead staining indicated that HPP hydrogel significantly reduced $H_2O_2$-induced chondrocyte death (Fig. 3k), with quantitative analysis further supporting this effect (Fig. 3l).The consistency between these experimental results confirms that HPP hydrogel effectively protects chondrocytes in an $H_2O_2$-rich environment. To assess long-term retention in both normal and OA joints in vivo, HPP hydrogels containing fluorescent markers were injected into the knee joints of healthy and OA mice. Fluorescence was monitored at various time points. In healthy mice, the fluorescent signal persisted at day 28, indicating incomplete degradation of the hydrogel. In contrast, OA mice exhibited a weaker fluorescent signal by day 21, with complete disappearance by day 28, indicating faster degradation in OA joints compared to normal joints (Fig. 3m). In summary, our findings demonstrate that HPP hydrogels exhibit excellent biosafety, efficient ROS scavenging capabilities, and robust long-term retention, establishing a strong foundation for future experimental investigations.

### Preparation, characterization, and biological properties of si-Fe-HPP

Building on the positive results obtained thus far, we incorporated si-Fe NPs into HPP hydrogels to create si-Fe-HPP composite hydrogels. We first prepared 100 μl of a 2.4% HA-PBA solution and added 20 μl of the si-Fe NPs solution, mixing thoroughly. Next, 40 μl of PVA was added, and the mixture was stirred to fabricate the composite hydrogel. The schematic preparation of si-Fe-HPP hydrogel is illustrated in Fig. 4a. The inversion experiment demonstrated the successful formation of the si-Fe-HPP hydrogel, which appeared as a yellow translucent solid gel with uniform color, indicating the homogeneous dispersion of si-Fe NPs within the HPP hydrogel (Fig. 4b). SEM images revealed a compact internal structure of the hydrogel, with si-Fe NPs evenly distributed and exhibiting good dispersion without significant particle agglomeration (Fig. 4c). The injectability of the si-Fe-HPP hydrogel is crucial for its potential as a biomedical material. The hydrogel could be smoothly injected through an insulin syringe, confirming its suitability for intra-articular drug delivery (Fig. 4d). Rheological testing showed that the storage modulus (G′) and loss modulus (G″) of the si-Fe-HPP hydrogel were higher than those of the HPP hydrogel alone, indicating that nanoparticle incorporation likely contributed to the enhanced hydrogel strength (Fig. 4e) [50]. The release behavior of Cy5-Fe NPs from the hydrogel in response to different $H_2O_2$ concentrations was monitored by measuring fluorescence intensity in the release medium (Fig. 4f). In the presence of 500 μM $H_2O_2$, the NPs exhibited a nearly 100% release rate by the fourth day, significantly faster than other groups. This $H_2O_2$-responsive characteristic is advantageous for adapting to the OA joint environment, allowing intelligent release of si-Fe NPs in response to changes in $H_2O_2$ levels. Figure S9 schematically illustrates the ROS scavenging and responsive behavior of the HPP hydrogel. $H_2O_2$ efficiently reacts with HPP, consuming $H_2O_2$ and breaking the crosslinking between PBA and PVA, leading to a disrupted hydrogel network, accelerated degradation, and nanoparticle release. The biocompatibility of the si-Fe-HPP composite gel was also evaluated. Whether varying the concentration of HPP hydrogel while keeping Fe concentration constant (Fig. 4g) or adjusting the concentration of si-Fe NPs while maintaining the HPP hydrogel concentration (Fig. 4h), none of the composite concentrations exhibited cytotoxicity. This indicates good compatibility of the si-Fe-HPP hydrogel with human chondrocytes. We then screened MMP-13 siRNA sequences from the literature for efficacy in silencing MMP-13 mRNA (Table S1) [13]. The selected mouse-derived MMP-13 siRNA sequences significantly reduced MMP-13 mRNA levels in mouse

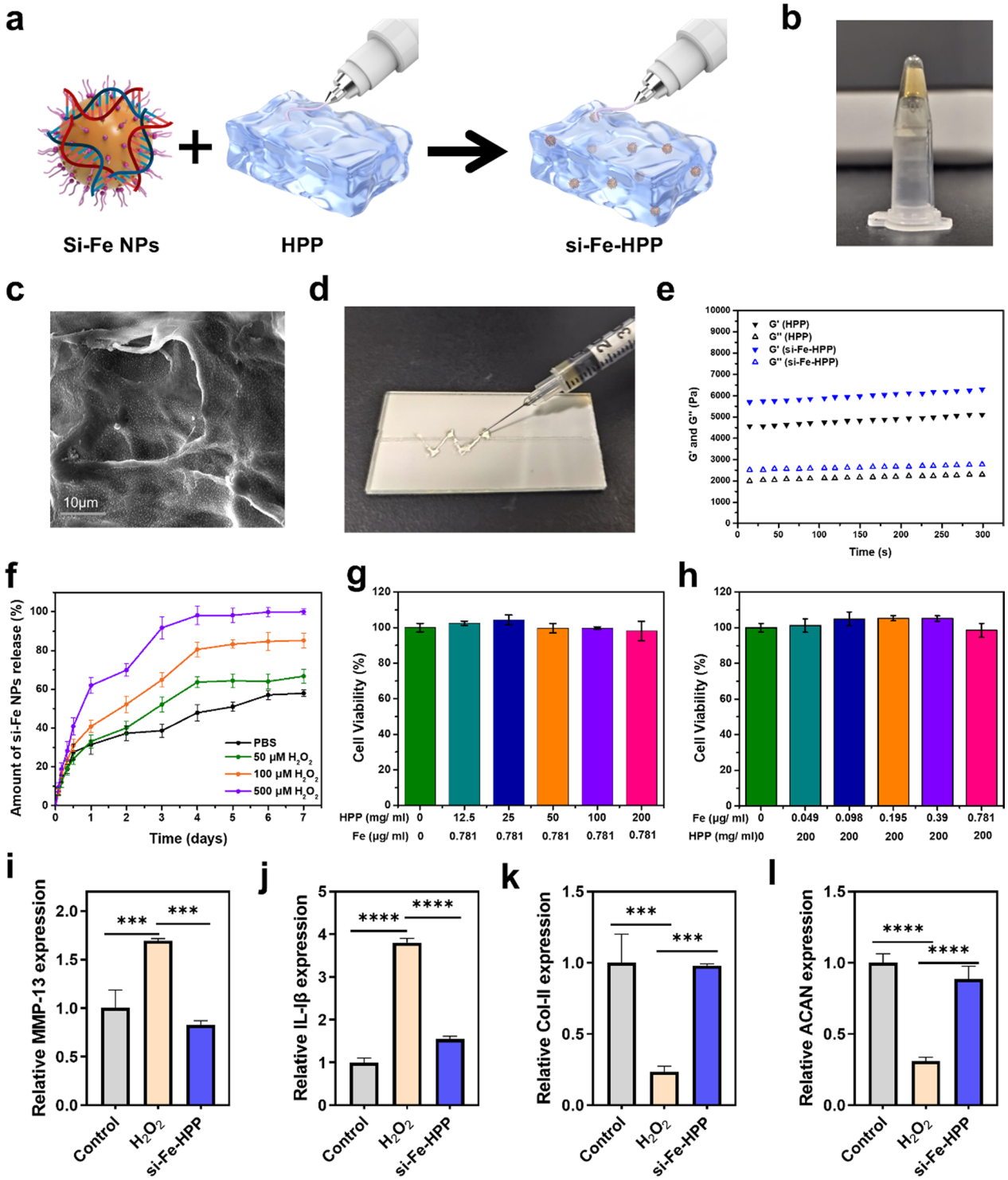


**Fig. 4** Preparation, characterization, and biological properties of si-Fe-HPP hydrogel. **a** Schematic diagram of preparation of si-Fe-HPP hydrogel. **b** Formation of si-Fe-HPP hydrogel. **c** SEM image of Si-Fe-HPP hydrogel. Scale bar: 10 μm. **d** Injectable properties of si-Fe-HPP hydrogel. **e** Rheological characterization of HPP hydrogel and si-Fe-HPP hydrogel. **f** Release behavior of si-Fe NPs in si-Fe-HPP hydrogel at various concentrations of $H_2O_2$. **g**–**h** Cell viabilities of C28/I2 cell line detected by MTT method at various concentrations of si-Fe-HPP hydrogel. **i**–**l** Evaluation of anti-inflammatory effect of si-Fe-HPP hydrogel on inflammation-induced C28/I2 cell line

4T1 cells, confirming robust silencing effects suitable for in vivo studies (Fig. S10). Furthermore, the effect of si-Fe-HPP on inflammation-induced chondrocytes was observed by using C28/I2 cell line. C28/I2 chondrocytes were divided into three groups: a blank medium group (as control), an $H_2O_2$ group, and an $H_2O_2$ + si-Fe-HPP hydrogel group. Cells were incubated for 6 h, after which the medium was replaced with complete medium for an additional 24-h incubation. Gene expression changes were then analyzed using RT-qPCR. RT-qPCR results showed that IL-1β and MMP-13 expression levels were significantly upregulated under inflammatory conditions, while the cartilage ECM synthesis-related genes ACAN and COL II were downregulated (Fig. 4i–l). The presence of si-Fe-HPP hydrogel significantly decreased the expression of IL-1β and MMP-13 compared to the inflammation-stimulated group (Fig. 4i–j). Additionally, si-Fe-HPP hydrogel inhibited the downregulation of ACAN and COL II, indicating its potential to prevent cartilage ECM degradation (Fig. 4k–l). The si-Fe-HPP hydrogel could help counter this downregulation by reducing oxidative stress and inflammation through ROS scavenging, as supported by previous studies [37, 51]. In conclusion, si-Fe-HPP exhibited excellent in vitro biocompatibility, robust gene silencing capabilities, and effective ROS scavenging properties, providing a strong foundation for future in vivo experiments.

#### si-Fe-HPP attenuated OA progression in vivo

To investigate the efficacy of si-Fe-HPP in attenuating the progression of OA, we utilized the DMM surgery-induced OA mouse model. Mice were randomly assigned to five groups: (1) Sham group; (2) DMM group; (3) DMM with HPP injection group; (4) DMM with si-Fe NPs injection group; and (5) DMM with si-Fe-HPP injection group. One week post-surgery, the si-Fe-HPP group received monthly intra-articular injections of 10 μL si-Fe-HPP (siMMP-13: 1.5 nmol/10 μL) over a 12-week period. Equivalent amounts of each component in si-Fe-HPP were administered to the HPP and si-Fe NPs groups, while the Sham and DMM groups received an equal volume of PBS. After 12 weeks of treatment, mice were euthanized, and joint tissues, major organs, and serum samples were collected for efficacy and safety assessment. Motor function was evaluated prior to euthanasia using the open field test, gait analysis, and Von Frey test (Fig. 5a). The results of Safranin-O/fast green (S.O.) and Alcian blue staining are depicted in (Fig. 5b). Quantitative assessments revealed that OA mice exhibited significant degenerative cartilage damage, evidenced by a substantial increase in Osteoarthritis Research Society International (OARSI) grading (Fig. 5c), along with decreased cartilage thickness (Fig. 5d), chondrocyte numbers (Fig. 5e), and relative cartilage area (Fig. 5f), compared to the Sham group. The degenerative changes included surface fibrosis, abnormal chondrocyte distribution, and extracellular matrix defects. In contrast to the DMM group, the si-Fe-HPP treatment effectively alleviated the OARSI score (Fig. 5c). S.O. and Alcian blue staining demonstrated that si-Fe-HPP significantly increased cartilage thickness (Fig. 5d), chondrocyte numbers (Fig. 5e), and relative cartilage area (Fig. 5f). Although the difference in S.O. staining between the HPP and si-Fe-HPP groups may appear less obvious, we believe it still reflects the complementary effects of the hydrogel and si-Fe NPs (Fig. 5b). The HPP hydrogel contributes additional benefits beyond ROS scavenging. By forming a lubricating layer within the joint, it reduces mechanical wear and enhances friction control and mechanical protection [52]. This friction-reducing property may partially explain the close S.O. staining levels observed between the two groups (with si-Fe-HPP demonstrating even better results actually), indicating that both treatments support cartilage protection. Moreover, the efficacy of si-Fe NPs treatment alone was lower than that of the HPP and si-Fe-HPP groups (Fig. 5b). One potential explanation is the lack of sustained local release with si-Fe NPs alone. Without the hydrogel matrix, siRNA may diffuse rapidly from the joint site, leading to suboptimal therapeutic concentrations over time [53]. Additionally, the absence of ROS scavenging and friction-reducing properties from the hydrogels could make joints more vulnerable to oxidative stress and mechanical damage. This increased susceptibility may weaken the protective effects observed with si-Fe NPs alone. Further immunohistochemical (IHC) staining revealed a significant reduction in MMP-13 expression in the si-Fe-HPP treated group, indicating effective inhibition of MMP-13 expression in chondrocytes (Fig. 5g–h). Additionally, the density of Col II in the OA mice treated with si-Fe-HPP was significantly increased, suggesting successful repair of the articular cartilage (Fig. 5i–j). In conclusion, these findings demonstrate that si-Fe-HPP is effective in slowing the progression of OA, presenting a promising treatment option.

#### si-Fe-HPP alleviated synovitis and subchondral bone sclerosis in vivo

Given that synovitis and subchondral bone sclerosis are characteristic pathological processes of OA, we further investigated the impact of si-Fe-HPP treatment on these processes in the context of delayed OA cartilage degeneration (Fig. 6a). First, we examined the body weight of treated mice. After 12 weeks of treatment, there were no significant differences in body weight changes among the five groups of mice (Fig. 6b). However, the diameter of the knee joints in the si-Fe-HPP-treated mice was

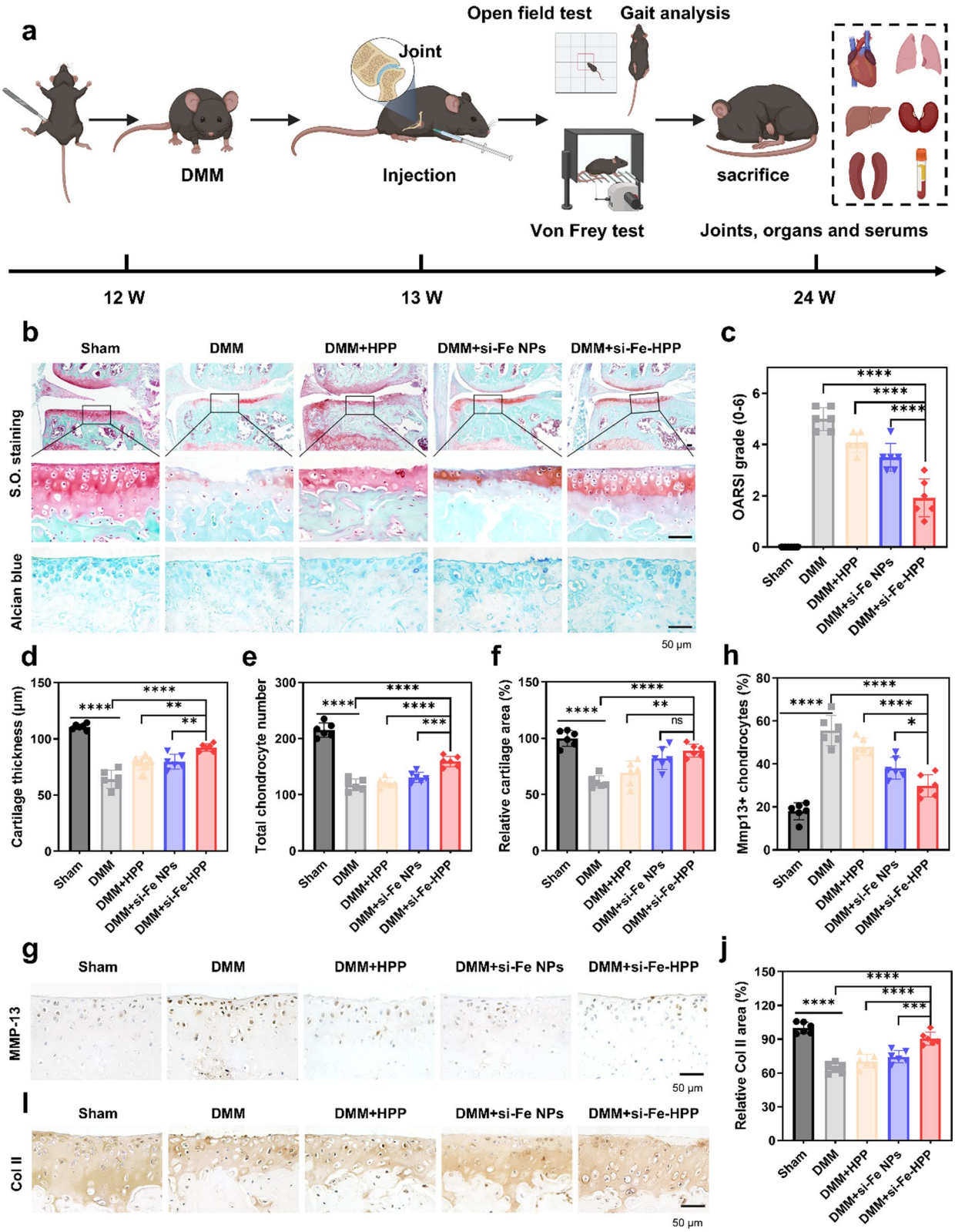


**Fig. 5** si-Fe-HPP attenuated OA progression in vivo. **a** Schematic diagram of the flow of animal experiment. **b**–**f** S.O. staining and Alcian blue staining (**b**) and quantification of Osteoarthritis Research Society International (OARSI) grading (**c**), cartilage thickness (**d**), chondrocyte number (**e**) and relative cartilage area (**f**). Scale bar: 50 μm. **g**–**j** Representative images of immunohistochemical staining of MMP-13 + (**g**) and Col II (**i**) in the cartilage of knee joints, as well as the relative quantification of MMP-13 + (**h**) and Col II (**j**). Scale bar: 50 μm. Data are expressed as mean ± SD

significantly reduced compared to the DMM group, with no statistically significant differences observed between the other groups (Fig. 6c). This indicates that si-Fe-HPP effectively reduced joint swelling. Additionally, hematoxylin and eosin (H&E) staining revealed substantial inflammatory cell infiltration and synovial thickening adjacent to the medial meniscus in DMM-operated mice (Fig. 6d). si-Fe-HPP treatment significantly attenuated inflammatory cell infiltration and reduced the synovitis score in the knee joint (Fig. 6e). These findings suggest that si-Fe-HPP effectively alleviated synovitis during OA progression.

Furthermore, microcomputed tomography (micro-CT) analysis, combined with three-dimensional (3D) reconstruction of the knee joints, demonstrated abnormal bone remodeling in the DMM group compared to the sham group (Fig. 6f). This was evidenced by narrowing of the articular space, uneven bony surfaces, and mineralization of the medial articulation, quantified by an increase in the number of osteophytes (Fig. 6g) and bone volume (BV) of the knee joints (Fig. 6h). si-Fe-HPP treatment significantly ameliorated these pathological changes. In the subchondral region, si-Fe-HPP treatment significantly reduced the DMM surgery-induced increases in subchondral bone plate (SBP) thickness (Fig. 6i), bone mineral density (BMD) (Fig. 6j), subchondral bone volume to tissue volume ratio (BV/TV) (Fig. 6k), trabecular number (Tb.N) (Fig. 6l), and trabecular thickness (Tb.Th) (Fig. 6m). Overall, the results demonstrate that si-Fe-HPP treatment has therapeutic effects on the typical pathological processes of OA progression, including synovitis and subchondral bone sclerosis, while also delaying cartilage degeneration (Fig. 6n). These findings highlight the potential of si-Fe-HPP as a promising treatment for OA.

#### si-Fe-HPP improved motor performance of OA mice

To assess the functional improvement of knee joints in OA mice following si-Fe-HPP treatment, we performed open field and gait analyses. During the 180-s testing period, OA mice exhibited reduced locomotor activity, shorter activity time, shorter activity distance, and slower average speed compared to the Sham group (Fig. 7a). As anticipated, si-Fe-HPP-treated mice demonstrated significantly improved locomotor performance, characterized by increased activity (Fig. 7b), extended activity time (Fig. 7c), longer activity distance (Fig. 7d), and higher average speed compared to other groups (Fig. 7e). These findings suggest that si-Fe-HPP effectively restored motor function in DMM surgery-induced OA mice. In the gait analysis, we used red ink to stain the front paws and blue ink for the hind paws, recording footprints as the mice walked along a 70 cm × 20 cm white track. In the Sham group, the footprints of the front and hind paws overlapped, whereas in the OA group, the footprints were markedly apart, indicating increased knee pain and walking difficulty post-DMM surgery (Fig. 7f). Remarkably, si-Fe-HPP treatment significantly improved the gait of OA mice, as evidenced by the quantitative analysis of stride length (blue dashed line) (Fig. 7g), step length (red dashed line) (Fig. 7h), and anterior and posterior imprint length (green dashed line) (Fig. 7i). In addition, the results of von Frey test showed that the si-Fe-HPP-treated paw withdrawal response thresholds were notably elevated, indicating reduced nociceptive sensitivity in mice (Fig. 7j). In conclusion, our comprehensive analysis reveals that si-Fe-HPP treatment not only restored motor function but also alleviated nociceptive sensitivity in DMM surgery-induced OA mice. These results underscore the therapeutic potential of si-Fe-HPP in OA treatment.

#### Excellent biocompatibility and safety of si-Fe-HPP in vivo

To ensure the biosafety of si-Fe-HPP hydrogel, H&E staining was performed on major organs, including the heart, liver, spleen, lungs, and kidneys of mice that received intra-articular injections of the hydrogel. The staining revealed no significant abnormalities, inflammation, or damage in any of the examined organs, indicating excellent biosafety of si-Fe-HPP (Fig. 8a). Furthermore, a comprehensive biochemical analysis was conducted to assess the systemic effects of si-Fe-HPP. Serum levels of alanine transaminase (ALT) (Fig. 8b), aspartate transaminase (AST) (Fig. 8c), albumin (ALB) (Fig. 8d), cholesterol (CHO) (Fig. 8e), blood urea nitrogen (BUN) (Fig. 8f), and lactate dehydrogenase (LDH) (Fig. 8g) were measured and found to be within the normal range across the Sham

(See figure on next page.)

**Fig. 6** si-Fe-HPP alleviated synovitis and subchondral bone sclerosis in OA mice. **a** Schematic diagram of HE staining and Micro-CT detection. **b**–**c** Body weight (**b**) and knee joint diameter (**c**) of mice at the endpoint of the animal experiment. **d**–**e** Representative images of H&E-stained mouse knee joint sections (**d**) and quantitative scores of synovitis (**e**). Scale bars: 50 μm. **f** Micro-CT analysis and 3D reconstructed images of mouse knee joints and sagittal views of the medial joint compartment showing changes in femoral and tibial surfaces and SBP thickness, respectively. Scale bars: 1 mm. **g**–**m** Quantification of the number of osteophytes (**g**), BV (**h**), SBP thickness (**i**), subchondral BMD (**j**), and the ratio of BV/TV (**k**), Tb.N (**l**), and Tb.Th (**m**) of the knee joint. **n** Schematic representation of the working mechanism of si-Fe-HPP in the knee joint of OA mice. Data are expressed as mean ± SD

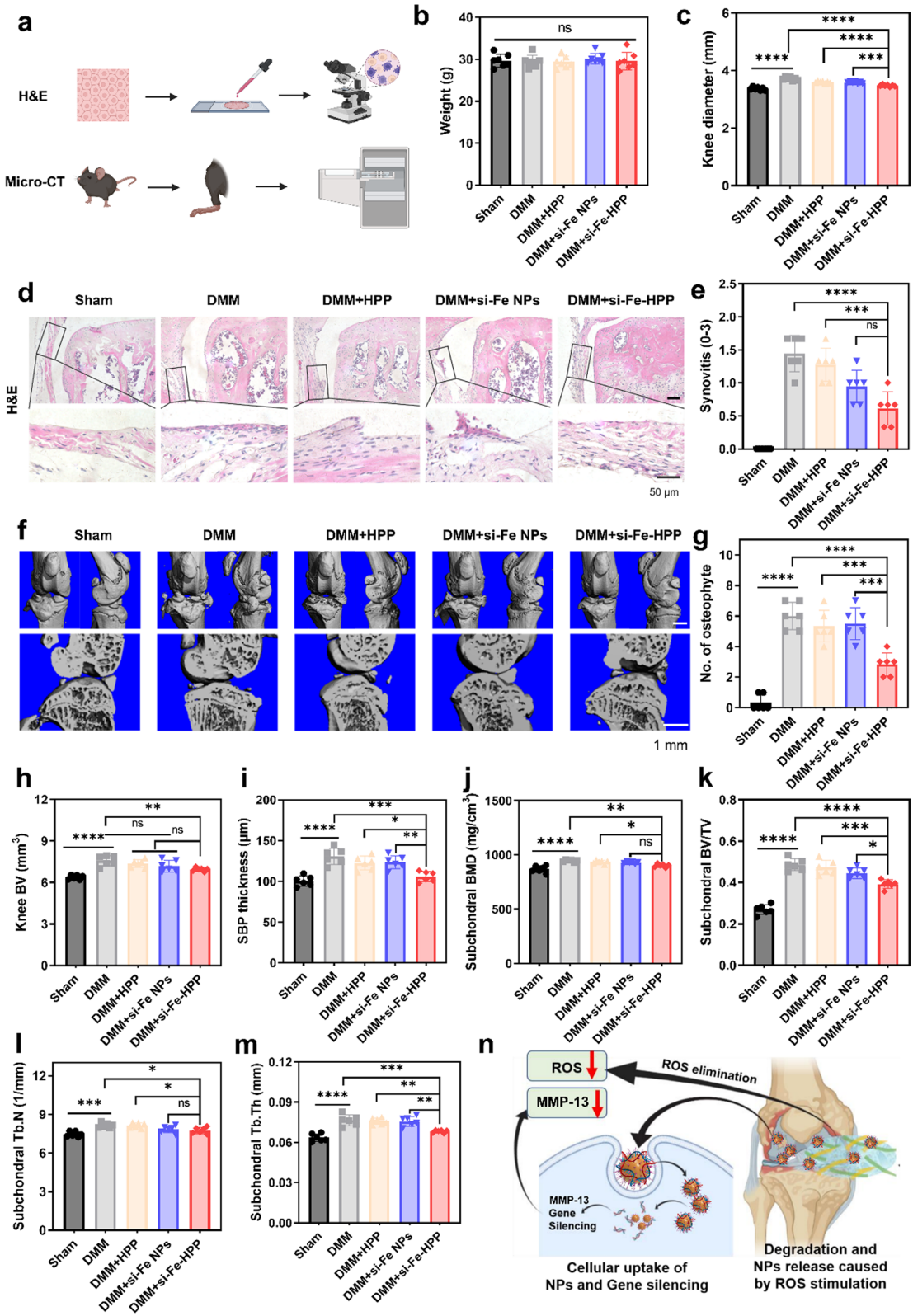


**Fig. 6** (See legend on previous page.)

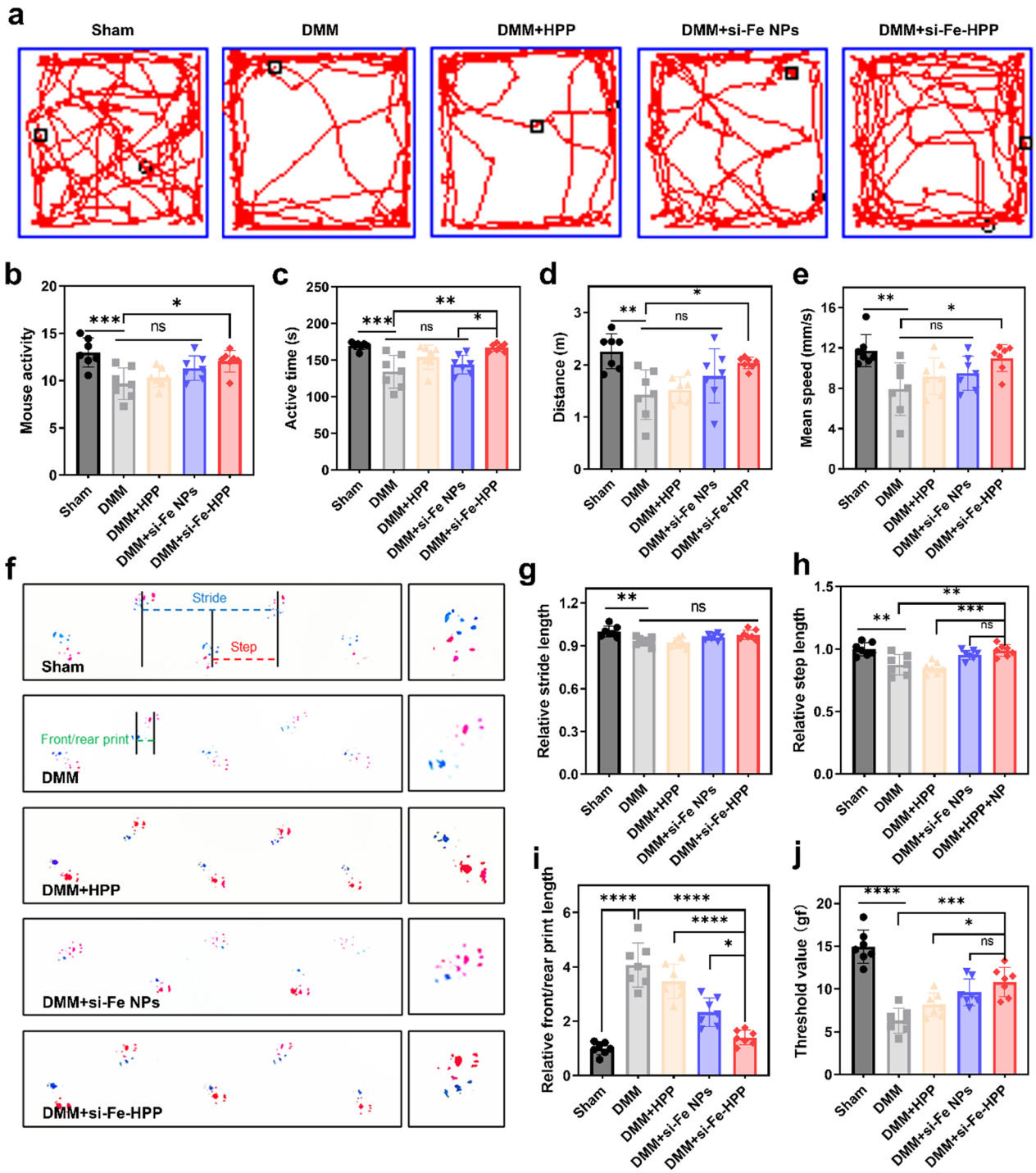


**Fig. 7** si-Fe-HPP improved the behavioral performance of mice. **a** A representative trajectory plot of the spontaneous activity of mice in the open field test. **b**–**e** the quantitative analyses of the relative activity (**b**), the duration of the activity (**c**), the distance traveled (**d**) and the average speed (**e**) of mice within the 180-s experimental period. **f** Gait analysis of mice. Dotted blue line, stride length; dotted red line, step length; dotted green line, front/aft footprint. Red footprint, forepaw; blue footprint, hindpaw. **g**–**i** Quantification of mouse footprints, including relative stride length (**g**), relative step length (**h**), and relative fore/rear footprint length (**i**). **j** Measurement of mechanical sensitivity of mice by the von Frey test. Data are expressed as mean ± SD

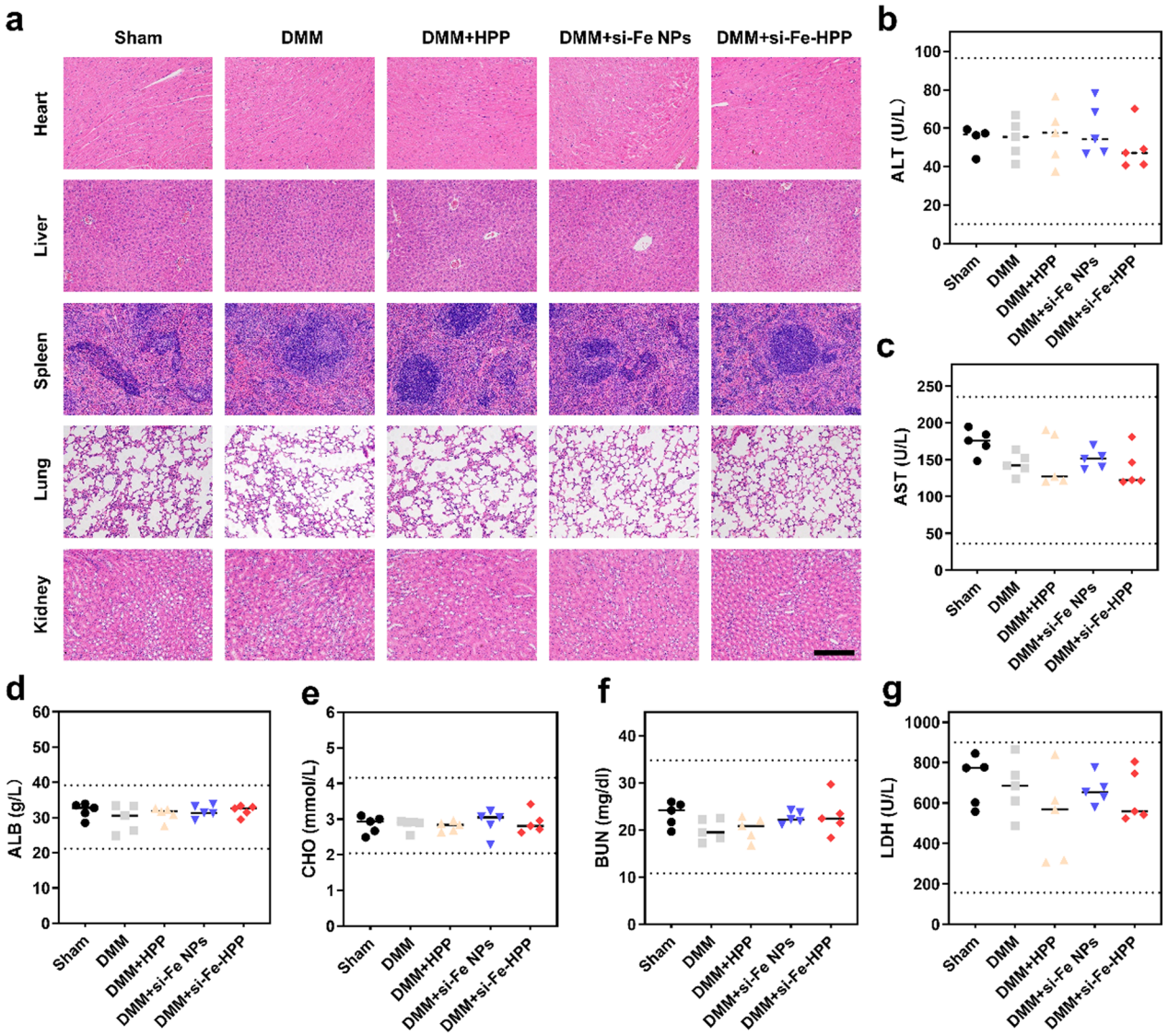


**Fig. 8** Satisfactory biocompatibility and safety of si-Fe-HPP in vivo. **a** Representative images of H&E staining of heart, liver, spleen, lung, kidney excised from mice treated with si-Fe-HPP hydrogel treatment and without treatment. Scale bars, 200 μm. **b**–**g** The levels of ALT (**b**), AST (**c**), ALB (**d**), CHO (**e**), BUN (**f**), and LDH (**g**) in serums from mice treated with si-Fe-HPP hydrogel and no treatment. The two dashed lines in figures represent the range of normal values for each serum biochemical index. Data are expressed as mean ± SD

group and the four experimental groups. These results confirm the good biocompatibility and safety profile of si-Fe-HPP in vivo. In summary, both histological and biochemical analyses demonstrate that si-Fe-HPP hydrogel exhibits excellent biosafety and biocompatibility. These findings provide strong evidence for the potential of si-Fe-HPP as a safe and effective therapeutic agent for the treatment of OA.

## Materials and methods

### Materials

Iron acetylacetonate, N,N-carbonyl diimidazole, oleylamine, oleic acid, calcium hydroxide, polyethyleneimine (Mw ~ 1800), hydroxy polyethylene glycol (Mw ~ 5000), sodium hyaluronate, and 3-aminobenzeneboronic acid were purchased from Aladdin Bioscience Co. (Shanghai, China). Fetal bovine serum, DMEM high glucose medium and other biologically related reagents or kits were purchased from KeyGen Biotechnology Co. (Nanjing, China).

### Preparation of $Fe_3O_4$ NPs

To synthesize iron nanoparticles, initially, 1.4 g of iron acetylacetonate was weighed and mixed with 8 mL of oleic acid and 12 mL of oleylamine. The reaction commenced by purging with $N_2$ at room temperature for 15 min, followed by vacuuming using an oil pump for 15 min while maintaining the nitrogen purge. The reaction mixture was heated to 120 °C and held for 2 h. Subsequently, the temperature was raised to 220 °C and maintained for 30 min, then increased at a rate of 2 °C/min to 300 °C and held for 30 min. The solution was cooled to 120 °C and kept for an additional 30 min. After cooling to 120 °C, nitrogen flow was stopped, and air was introduced to continue the reaction for 90 min. Upon completion, the heating was turned off, and the liquid was transferred to a 50 mL centrifuge tube. Acetone (50 mL) was added, and centrifugation at 8000 rpm for 5 min separated the supernatant, which was discarded. The precipitate was dissolved in 5–10 mL of hexane, followed by addition of 40 mL of ethanol and repeated centrifugation. This washing process was repeated twice. Finally, the nanoparticles were dissolved in 5 mL of hexane, sealed, and stored at room temperature.

### Preparation of PEI-PEG

Anhydrous and alcohol-free chloroform solvent was prepared by initially mixing chloroform with deionized water, subjecting it to triple extraction, and treating it with calcium hydride under reflux at 65 ℃ for 4 h to obtain redistilled chloroform. In the subsequent step, HO-PEG2000-OH was activated by combining 2 g of HO-PEG2000-OH with 0.821 g of CDI in 20 mL of the prepared chloroform solvent, stirring overnight under a nitrogen atmosphere, and precipitating the resulting PEG-CDI with cold ether followed by vacuum drying. Further, 1.4 g of PEG-CDI and 1.9 g of PEI (Mw ≈ 1800 Da) were dissolved in 7.5 mL of chloroform, mixed, and reacted for 12 h under nitrogen. The product, PEI-PEG, was obtained after precipitation with cold ether, washing, and vacuum drying, and stored at −20 ℃. Structural confirmation was performed by dissolving 5 mg of PEI-PEG in 500 μL of deuterated chloroform ($CDCl_3$), transferring it to an NMR tube, and analyzing its structure using 1H NMR spectroscopy.

### Preparation of $Fe_3O_4$-PEI-PEG NPs

$Fe_3O_4$ nanoparticles (20–30 μL), dispersed in hexane, were transferred to an EP tube and ethanol was added to induce precipitation. After centrifugation, the supernatant was discarded, and the precipitate was purged with nitrogen, dried, and weighed to determine the nanoparticle mass. The nanoparticles were then redispersed in chloroform and mixed with a PEI-PEG solution, followed by sonication for 30 min to 1 h and overnight shaking. The resulting mixture was dried using rotary evaporation and further subjected to vacuum drying for 24 h. The product was subsequently dispersed in water via sonication and subjected to dialysis for three days with three changes of dialysate. Finally, the product was stored under sealed conditions.

### Determination of total iron concentration in $Fe_3O_4$-PEI-PEG NPs

A small volume (approximately 10 μL) of nanoparticles was treated with nitric acid and heated to 200 °C, with continuous shaking to prevent evaporation. Upon evaporation of most of the nitric acid, the residue was diluted with water, and the dilution factor was recorded. Phenanthroline and hydroxylamine hydrochloride were dissolved in acetic acid-ammonium acetate solution and 2M hydrochloric acid, and added to an EP tube. After incubating for 2 h in the dark, the solution was transferred to a 96-well plate and the absorbance was measured. The iron concentration of the sample was determined from a standard curve, and multiplied by the dilution factor to obtain the total iron concentration of the original sample.

### $Fe_3O_4$-PEI-PEG NPs loaded siRNA method

A solution of 1 $OD_{260}$ of siRNA (approximately 33 μg) (Shanghai GenePharma Co., Ltd.) was dissolved in 40 μL DEPC water. The concentration of siRNA was precisely measured using a μDrop Plate (Thermo Scientific™, USA) to determine the nucleic acid concentration. $Fe_3O_4$-PEI-PEG NPs were diluted accordingly, and a proportional volume was aspirated using a pipette. The NP solution was then added dropwise to the siRNA solution while gently mixing with a pipette gun. The mixture was thoroughly blended and allowed to stand at room temperature for 30 min to form complexes of siRNA and $Fe_3O_4$-PEI-PEG NPs (si-Fe NPs).

### Evaluation of the ability of $Fe_3O_4$-PEI-PEG NPs to protect siRNAs

Free siRNA and si-Fe NPs were mixed with various concentrations of RNA degrading enzyme (RNase) in 0.2 mL EP tubes, sealed with film, and incubated for 1 h in a 37 °C water bath. Subsequently, gel electrophoresis was conducted.

### Evaluation of cellular uptake capacity of si-Fe NPs

The C28/I2 cell line was divided into two groups in a 24-well plate: the naked siRNA group and the siRNA-Fe NPs group. For the siRNA-Fe NPs group (siRNA: 80 pmol/mL), FAM-siNC-Fe NPs were prepared, while equal amounts of free FAM-siNC were used for the free siRNA group. Cells were incubated in 24-well plates

for 12 h, followed by medium aspiration and two PBS washes to remove extracellular free siRNA or nanoparticles. Next, 200 μl of 4% paraformaldehyde was added for fixation. After fixation, the cells were washed twice with PBS and stained with 200 μl of DAPI solution. Following 2–3 PBS washes, fluorescence microscopy was used for observation.

### Preparation of HA-PBA polymers

HA (2 g) was dissolved in 200 mL of deionized water and stirred overnight until fully dissolved, yielding a clear and viscous liquid solution. Subsequently, PBA (940 mg) was dissolved in 20 mL of deionized water under sonication until complete dissolution. This solution was then combined with the HA solution. The pH of the resulting solution was adjusted to 6.5~7 using 1 M NaOH and 1 M hydrochloric acid solutions. DMTMM (1.6 g) was then dissolved in 10 mL of deionized water by ultrasonication, followed by mixing with the HA + PBA solution. The reaction mixture was stirred at room temperature under a nitrogen atmosphere for 72 h.

#### *Preparation of HPP hydrogels in different ratios*

Firstly, PVA solutions of different concentrations were prepared. PVA (9 g) was added to 100 mL of deionized water and heated to 90 ℃ to dissolve. After cooling to room temperature, the solution was transferred to a sample bottle, resulting in a 9% (w/v) PVA solution. Portions of this solution were diluted to obtain 3 and 6% PVA solutions with deionized water. Next, HA-PBA solutions of varying concentrations were prepared. HA-PBA samples (2, 4, and 6 mg) were individually weighed into 1.5 mL EP tubes. To dissolve the samples, 200 μL of PBS was added to each tube, followed by continuous sonication. This process yielded 1, 2, and 3% (w/v) HA-PBA solutions in total. Subsequently, 66.7 μL of 3, 6, and 9% PVA solution was added to corresponding portions of the HA-PBA solutions. A pipette gun was used to mix the PVA solution into the HA-PBA solution while stirring, ensuring thorough mixing before continuing stirring to maintain uniformity. After stirring for 5–10 s, the liquid in the EP tube condensed into a viscous solid. The mixture was then centrifuged at 10,000 rpm for 3 min to remove air bubbles. Successful formation of the HPP hydrogel was confirmed by inverting the EP tube; no liquid flow indicated successful gelation.

#### *Hydrogel rheology testing*

The HPP and si-Fe-HPP hydrogel were molded into cylinders with a diameter of 8 mm and height of 2 mm using a PTFE mold. These cylinders were carefully removed and positioned on the base plate of a rheometer. Subsequently, a series of rheological tests were conducted using the rheometer. A strain sweep was performed to evaluate the response over a strain range of 0.1–1000% at a fixed angular velocity frequency of 1 Hz. An angular velocity frequency sweep followed, maintaining a strain of 1% while scanning angular velocities from 0.1 to 20 Hz. A time sweep was conducted at 1% strain and 1 Hz frequency, spanning 120 s with time as the x-axis. Lastly, a step strain test involved varying strains (1–1000%) at 1 Hz frequency, with each strain step lasting 2 min. These tests aimed to characterize the mechanical properties and viscoelastic behavior of the hydrogel formulations under different conditions, providing insights into their potential applications in biomedical settings.

#### *In vitro degradation of hydrogels with different ratios of HPP*

Nine different hydrogel formulations were prepared with varying ratios of HA-PBA and PVA: 1% HA-PBA + 3% PVA (denoted as 1% + 3%, and so forth), up to 3% HA-PBA + 9% PVA. Each formulation was duplicated, resulting in a total of 18 hydrogel samples. Initially, each hydrogel sample was immersed in 2 mL of PBS to reach swelling equilibrium, and the initial weight was recorded. Subsequently, pairs of hydrogels with identical compositions were separately incubated in 2 mL of PBS and 2 mL of 100 μM $H_2O_2$ solution at 37 °C. Every 48 h, the incubation medium was replaced, and the hydrogels were gently centrifuged at low speed. After removing the liquid, the surface of each hydrogel was dried with filter paper, reweighed, and the weight recorded. This process was repeated until complete degradation of the hydrogel occurred in the PBS medium. These experiments were conducted to assess the degradation behavior of the HPP hydrogels under oxidative conditions, mimicking environments relevant to biomedical applications.

#### *Investigation of ROS-responsive degradation behavior of HPP hydrogels*

Four identical HPP hydrogel samples (2% + 9%) were prepared and individually placed into separate 2 mL EP tubes. Each hydrogel sample was initially immersed in 2 mL of PBS until swelling equilibrium was reached. The initial weight of each hydrogel was recorded as 100%. Subsequently, the PBS was replaced with solutions containing 50 μM $H_2O_2$, 100 μM $H_2O_2$, and 500 μM $H_2O_2$ in separate EP tubes containing one hydrogel sample each. The samples were then incubated at 37 °C, and every 48 h, they were gently centrifuged at low speed. After removing the supernatant, the surface of each HPP hydrogel was carefully dried with filter paper, reweighed, and the weight recorded. The incubation medium (PBS or $H_2O_2$ solution) was replenished after each measurement, and the process was repeated until complete degradation

of the HPP hydrogel was observed under the respective conditions. This experimental setup aimed to evaluate the degradation kinetics of the HPP hydrogel under oxidative stress conditions induced by varying concentrations of $H_2O_2$, simulating environments relevant to biomedical applications.

#### *Investigation of $H_2O_2$ scavenging capacity of HPP hydrogel in vitro*

Four different concentrations of $H_2O_2$ solution (50, 100, 500 μM, 1 mM) were prepared in duplicate in 1.5 mL EP tubes, totaling eight samples, each with a volume of 500 μL. One hundred microliters (100 μL) of HPP hydrogel was immersed in each $H_2O_2$ solution and incubated at room temperature for 2 h in darkness. Subsequently, the hydrogel samples were centrifuged to collect 100 μL of the supernatant, which was then transferred to a 96-well plate. To this, an equal volume of 1 M aqueous sodium iodide solution was added and allowed to react for five minutes in the absence of light. UV absorption spectra were then measured using a spectrophotometer within the wavelength range of 300~500 nm to analyze the reaction products formed under oxidative conditions induced by different concentrations of $H_2O_2$. This methodological approach aimed to assess the oxidative degradation behavior of the HPP hydrogel and characterize its response to varying levels of oxidative stress.

#### *Cell compatibility*

C28/I2 cells were seeded into 96-well plates. Si-Fe nanoparticles (NPs) were prepared at various concentrations based on iron mass, dispersed in complete medium, and added to the 96-well plates. Final concentrations of iron (Fe) in the wells were adjusted to 0, 0.049, 0.088, 0.195, 0.390, and 0.781 μg/mL, with each concentration tested in triplicate wells. The same experimental setup was applied to HPP and si-Fe-HPP hydrogels. This approach ensured consistent testing across different materials (Si-Fe NPs, HPP, and si-Fe-HPP hydrogels).

#### *RT-qPCR*

Cellular mRNA was extracted from chondrocytes following the manufacturer's instructions using the RNA-quick Purification Kit (#RN001, ES Science, Shanghai, China). The HiScript-TS 5′/3′ RACE Kit (RA101, Vazyme, China) was utilized for the detection of MMP-13, IL-1β, ACAN, and Col II expression levels. RT-qPCR analysis was conducted on a LightCycler 480 PCR system (Roche, Switzerland) using ChamQ Universal SYBR qPCR Master Mix (Q711, Vazyme, China). Primer sequences for the assays are provided in Table S2.

#### *Animal experiments*

All animal experiments were conducted with the approval of the Ethics Committee of Drum Tower Hospital affiliated with Nanjing University. The experiments adhered strictly to the ARRIVE guidelines and were carried out in compliance with the U.K. Animals (Scientific Procedures) Act of 1986 and associated guidelines, EU Directive 2010/63/EU for animal experiments, and the National Institutes of Health Guide for the Care and Use of Laboratory Animals (NIH Publications No. 8023, revised 1978). Male 12-week-old C57BL/6 mice were procured from the Animal Model Research Center of Nanjing University and were housed under specific pathogen-free conditions with ad libitum access to food and water. The OA mouse model was induced by surgical destabilization of the medial meniscus under isoflurane anesthesia. Twelve-week-old male C57BL/6 mice were prepped by sterilizing the skin with iodophor. During surgery, the joint cavity of the right knee was opened, and the medial meniscotibial ligament was severed to destabilize the medial meniscus from the tibial plateau under a stereomicroscope. Loosening was confirmed using microscopic forceps, after which the incision was sutured layer by layer and sterilized again. The same surgical procedure was performed on the Sham group without ligament resection. Following Sham or DMM surgery on the right knee joint, mice were randomly allocated into five groups: (1) Sham group; (2) DMM group; (3) DMM with HPP injection group; (4) DMM with si-Fe NPs injection group; and (5) DMM with si-Fe-HPP injection group. One week post-surgery, the si-Fe-HPP group received intra-articular injections of 10 μL si-Fe-HPP (siMMP-13: 1.5 nmol/10 μL) once per month for a period of 12 weeks. The HPP and si-Fe NPs groups were administered equivalent amounts of their respective components found in si-Fe-HPP, while the Sham and DMM control groups received an equal volume of PBS. After 12 weeks of treatment, mice were euthanized, and joint tissues, major organs, and serum samples were collected for efficacy and safety evaluation. Motor function was assessed using the open field test, gait analysis, and Von Frey test before the animals were sacrificed for sampling (Fig. 5a).

#### *Histological analysis*

A 10% ethylenediaminetetraacetic acid (EDTA) solution (#1340, Biofroxx, Germany) was utilized for decalcifying mouse knee joints, followed by embedding in paraffin blocks. The knee joints were sectioned coronally into

continuous 5 μm slices using a microtome (Thermo, Germany). Sections were subjected to H&E staining (#C0105S, Beyotime) and S.O. staining (#G1371, Solarbio) to evaluate synovitis and cartilage lesions, respectively. Synovitis severity was assessed using a scoring system ranging from 0 to 3, and cartilage degeneration was evaluated using the Osteoarthritis Research Society International (OARSI) grading system (0–6) by two independent blinded observers. The maximum scores for synovitis and OARSI were recorded, and their average values were calculated. Furthermore, to assess the in vivo biocompatibility of si-Fe-HPP, sections of major organs (heart, liver, spleen, lungs, and kidneys) were stained with H&E (#C0105S, Beyotime). Serum biochemical indicators were also analyzed to evaluate safety profiles.

#### *Immunohistochemical staining*

Endogenous peroxidase activity was quenched using 3% (v/v) $H_2O_2$. Horseradish peroxidase-conjugated secondary antibodies, specifically goat anti-rabbit or anti-mouse immunoglobulin G (IgG) (Biosharp, Shanghai, China), were used. Immunohistochemical staining was visualized using the Ultrasensitive DAB kit (#1205250, Typing, Nanjing, China). Non-immune IgG served as a negative control during the immunohistochemical staining process.

#### *Micro-CT analysis*

Micro-CT scans were conducted using a VivaCT 80 scanner (Scanco Medical AG, Switzerland) equipped with a 70 kVp light source. 3D reconstructions of mouse knee joints were generated using Scanco Medical software (Scanco, Switzerland) with a threshold set at 220 to evaluate bone morphology. Quantitative analysis of osteophyte formation was performed based on the 3D reconstructed images.

#### *Behavior tests*

The open field test was conducted in a 50 cm × 50 cm square arena with 25 cm high walls under quiet, dimly-lit conditions. Mice movement trajectories were recorded using a tracking system (Zhenghua Technology). For gait analysis, mice freely walked on a 70 cm × 20 cm white runway. Prior to testing, the forepaws were marked with red ink and hindpaws with blue ink to record footprints. Measurements were analyzed by two independent observers blinded to the experimental conditions. Pain sensitivity was assessed using an electronic von Frey anesthesiometer (IITC, Woodland Hills, USA), recording the mechanical paw withdrawal threshold.

#### *Statistical analysis*

Statistical analyses were conducted using GraphPad Prism software (version 8.0) and SPSS software (version 25.0). Quantitative results represent findings from at least three independent experiments. Graphical Analysis Using GraphPad Prism 8.0 and Origin 2022. No samples or animals were excluded from the analysis. To assess data variance equality and normal distribution, Levene's test and Shapiro–Wilk's test were applied, respectively. For comparisons among multiple groups, either one-way or two-way analysis of variance (ANOVA) followed by Tukey's post hoc test was performed. Data are presented as mean ± standard deviation, and statistical significance was set at $P < 0.05$.

## Conclusion

In summary, a bifunctional si-Fe-HPP hydrogels with excellent ROS scavenging ability and RNAi therapeutic properties were prepared by incorporation of si-Fe NPs into HPP hydrogels. In vitro investigations demonstrated that si-Fe-HPP exhibits excellent biocompatibility, strong anti-inflammatory activity, and prolonged stability and retention time within the knee joint. In vivo, si-Fe-HPP significantly attenuated cartilage degradation in DMM-induced OA mice, which was evidenced by alleviation of synovitis, osteophyte formation, subchondral bone sclerosis as well as improvement in physical activity and reduced pain. Overall, the multifunctional si-Fe-HPP hydrogel with great abilities to protect chondrocytes and attenuate OA progression could serve as a potential therapeutic material for OA treatment.

## Supplementary Information

The online version contains supplementary material available at https://doi.org/10.1186/s12951-024-03046-7.

Additional file 1.

**Acknowledgements**
Not applicable.

**Author contributions**
Qiuyang Wang, Kai Feng and Guangsheng Wang contributed equally to this work. Q.W., K.F. and G.W. designed and performed all experiments. J.J. assisted with the cell experiments. W.L. aided in the animal experiments. Q.W. drafted the manuscript. P.W., X.S. and W.W. provided critical feedback on the manuscript. P.W. and Q.J. edited the manuscript and supervised the entire project. All authors reviewed and approved the final manuscript.

**Funding**
This work was supported by the National Basic Research Program of China (2021YFA1201404), National Natural Science Foundation of China (32271413), Jiangsu Provincial Key Medical Center Foundation, Jiangsu Provincial Medical Outstanding Talent Foundation, Jiangsu Provincial Medical Youth Talent Foundation and Jiangsu Provincial Key Medical Talent Foundation. The Fundamental Research Funds for the Central Universities (14380493, 14380494).

**Data availability**
No datasets were generated or analysed during the current study.

## Declarations

**Ethics approval and consent to participate**
All animal experiments were conducted with the approval of the Ethics Committee of Drum Tower Hospital, affiliated with Nanjing University.

**Consent for publication**
All authors of this study agreed to publish.

**Competing interests**
The authors declare no competing interests.

**Author details**
[1]State Key Laboratory of Pharmaceutical Biotechnology, Division of Sports Medicine and Adult Reconstructive Surgery, Department of Orthopedic Surgery, Nanjing Drum Tower Hospital, The Affiliated Hospital of Nanjing University Medical School, 321 Zhongshan Road, Nanjing 210008, People's Republic of China. [2]Branch of National Clinical Research Center for Orthopedics, Sports Medicine and Rehabilitation, Nanjing 210008, People's Republic of China. [3]Co-Innovation Center of Neuroregeneration, Nantong University, Nantong 226019, People's Republic of China. [4]State Key Laboratory of Natural Medicines, Key Laboratory of Drug Quality Control and Pharmacovigilance, School of Pharmacy, China Pharmaceutical University, Nanjing 210009, People's Republic of China. [5]Children's Hospital of Nanjing Medical University, Nanjing 210008, People's Republic of China.

Received: 4 July 2024 Accepted: 29 November 2024
Published online: 16 January 2025

**References**

1. Kamatsuki Y, Furumatsu T, Hiranaka T, Okazaki Y, Kintaka K, Kodama Y, Miyazawa S, Ozaki T. Epidemiological features of acute medial meniscus posterior root tears. Int Orthop. 2023;47:2537–45.
2. Li W, Lv Z, Wang P, Xie Y, Sun W, Guo H, Jin X, Liu Y, Jiang R, Fei Y, et al. Near infrared responsive gold nanorods attenuate osteoarthritis progression by targeting TRPV1. Adv Sci. 2024;11:e2307683.
3. Lv Z, Wang P, Li W, Xie Y, Sun W, Jin X, Jiang R, Fei Y, Liu Y, Shi T, et al. Bifunctional TRPV1 targeted magnetothermal switch to attenuate osteoarthritis progression. Research. 2024;7:0316.
4. Kang D, Lee J, Jung J, Carlson BA, Chang MJ, Chang CB, Kang SB, Lee BC, Gladyshev VN, Hatfield DL, et al. Selenophosphate synthetase 1 deficiency exacerbates osteoarthritis by dysregulating redox homeostasis. Nat Commun. 2022;13:779.
5. Glyn-Jones S, Palmer AJ, Agricola R, Price AJ, Vincent TL, Weinans H, Carr AJ. Osteoarthritis. Lancet. 2015;386:376–87.
6. Bijlsma JW, Berenbaum F, Lafeber FP. Osteoarthritis: an update with relevance for clinical practice. Lancet. 2011;377:2115–26.
7. Rainsford KD. Profile and mechanisms of gastrointestinal and other side effects of nonsteroidal anti-inflammatory drugs (NSAIDs). Am J Med. 1999; 107:27S–35S; discussion 35S–36S.
8. Yu J, Wang W, Jiang Z, Liu H. TPX2 upregulates MMP13 to promote the progression of lipopolysaccharide-induced osteoarthritis. PeerJ. 2024;12:e17032.
9. Wang T, He C. Pro-inflammatory cytokines: the link between obesity and osteoarthritis. Cytokine Growth Factor Rev. 2018;44:38–50.
10. Lv Z, Xu X, Sun Z, Yang YX, Guo H, Li J, Sun K, Wu R, Xu J, Jiang Q, et al. TRPV1 alleviates osteoarthritis by inhibiting M1 macrophage polarization via Ca2+/CaMKII/Nrf2 signaling pathway. Cell Death Dis. 2021;12:504.
11. Diekman BO, Loeser RF. Aging and the emerging role of cellular senescence in osteoarthritis. Osteoarthritis Cartilage. 2024;32:365–71.
12. Zhang W, Zhang C, Luo C, Zhan Y, Zhong B. Design, cyclization, and optimization of MMP13-TIMP1 interaction-derived self-inhibitory peptides against chondrocyte senescence in osteoarthritis. Int J Biol Macromol. 2019;121:921–9.
13. Bedingfield SK, Colazo JM, Yu F, Liu DD, Jackson MA, Himmel LE, Cho H, Crofford LJ, Hasty KA, Duvall CL. Amelioration of post-traumatic osteoarthritis via nanoparticle depots delivering small interfering RNA to damaged cartilage. Nat Biomed Eng. 2021;5:1069–83.
14. Yao X, Sun K, Yu S, Luo J, Guo J, Lin J, Wang G, Guo Z, Ye Y, Guo F. Chondrocyte ferroptosis contribute to the progression of osteoarthritis. J Orthop Translat. 2021;27:33–43.
15. Zhang ZJ, Hou YK, Chen MW, Yu XZ, Chen SY, Yue YR, Guo XT, Chen JX, Zhou Q. A pH-responsive metal-organic framework for the co-delivery of HIF-2α siRNA and curcumin for enhanced therapy of osteoarthritis. J Nanobiotechnol. 2023;21:18.
16. Alterman JF, Godinho B, Hassler MR, Ferguson CM, Echeverria D, Sapp E, Haraszti RA, Coles AH, Conroy F, Miller R, et al. A divalent siRNA chemical scaffold for potent and sustained modulation of gene expression throughout the central nervous system. Nat Biotechnol. 2019;37:884–94.
17. Kulkarni JA, Witzigmann D, Chen S, Cullis PR, van der Meel R. Lipid nanoparticle technology for clinical translation of siRNA therapeutics. Acc Chem Res. 2019;52:2435–44.
18. Biscans A, Coles A, Haraszti R, Echeverria D, Hassler M, Osborn M, Khvorova A. Diverse lipid conjugates for functional extra-hepatic siRNA delivery in vivo. Nucleic Acids Res. 2019;47:1082–96.
19. Elbashir SM, Harborth J, Lendeckel W, Yalcin A, Weber K, Tuschl T. Duplexes of 21-nucleotide RNAs mediate RNA interference in cultured mammalian cells. Nature. 2001;411:494–8.
20. Mahmood ur R, Ali I, Husnain T, Riazuddin S: RNA interference: the story of gene silencing in plants and humans. Biotechnol Adv. 2008;26:202–9.
21. Iwakawa HO, Tomari Y. Life of RISC: Formation, action, and degradation of RNA-induced silencing complex. Mol Cell. 2022;82:30–43.
22. Reynolds A, Leake D, Boese Q, Scaringe S, Marshall WS, Khvorova A. Rational siRNA design for RNA interference. Nat Biotechnol. 2004;22:326–30.
23. O'Brien TJ, Hollinshead F, Goodrich LR. Extracellular vesicles in the treatment and prevention of osteoarthritis: can horses help us translate this therapy to humans? Extracell Vesicles Circ Nucl Acids. 2023;4:151–69.
24. Setten RL, Rossi JJ, Han SP. The current state and future directions of RNAi-based therapeutics. Nat Rev Drug Discov. 2019;18:421–46.
25. Pecot CV, Calin GA, Coleman RL, Lopez-Berestein G, Sood AK. RNA interference in the clinic: challenges and future directions. Nat Rev Cancer. 2011;11:59–67.
26. Zhang L, Peng H, Zhang W, Li Y, Liu L, Leng T. Yeast cell wall particle mediated nanotube-RNA delivery system loaded with miR365 antagomir for post-traumatic osteoarthritis therapy via oral route. Theranostics. 2020;10:8479–93.
27. Zheng L, Zhuang Z, Li Y, Shi T, Fu K, Yan W, Zhang L, Wang P, Li L, Jiang Q. Bone targeting antioxidative nano-iron oxide for treating postmenopausal osteoporosis. Bioact Mater. 2022;14:250–61.
28. Zhang Y, Wang P, Mao H, Zhang Y, Zheng L, Yu P, Guo Z, Li L, Jiang Q. PEGylated gold nanoparticles promote osteogenic differentiation in in vitro and in vivo systems. Mater Des. 2021;197:109231.
29. Wang P, Wang Q, Wu D, Zhang Y, Kang S, Wang X, Gu J, Wu H, Xu Z, Jiang Q. Enhancing osteogenic bioactivities of coaxial electrospinning nanoscaffolds through incorporating iron oxide nanoparticles and icaritin for bone regeneration. Nano Res. 2024.
30. Malek A, Czubayko F, Aigner A. PEG grafting of polyethylenimine (PEI) exerts different effects on DNA transfection and siRNA-induced gene targeting efficacy. J Drug Target. 2008;16:124–39.
31. Fattahi N, Gorgannezhad L, Masoule SF, Babanejad N, Ramazani A, Raoufi M, Sharifikolouei E, Foroumadi A, Khoobi M. PEI-based functional materials: fabrication techniques, properties, and biomedical applications. Adv Colloid Interface Sci. 2024;325:103119.
32. Zhang J, Zhu J, Zhao L, Mao K, Gu Q, Li D, Zhao J, Wu X. RGD-modified multifunctional nanoparticles encapsulating salvianolic acid A for targeted treatment of choroidal neovascularization. J Nanobiotechnology. 2021;19:196.
33. Li Y, Li C, Yan J, Liao Y, Qin C, Wang L, Huang Y, Yang C, Wang J, Ding X, et al. Polymeric micellar nanoparticles for effective CRISPR/Cas9 genome editing in cancer. Biomaterials. 2024;309:122573.
34. Arra M, Swarnkar G, Ke K, Otero JE, Ying J, Duan X, Maruyama T, Rai MF, O'Keefe RJ, Mbalaviele G, et al. LDHA-mediated ROS generation in chondrocytes is a potential therapeutic target for osteoarthritis. Nat Commun. 2020;11:3427.

35. Liu L, Zhang W, Liu T, Tan Y, Chen C, Zhao J, Geng H, Ma C. The physiological metabolite α-ketoglutarate ameliorates osteoarthritis by regulating mitophagy and oxidative stress. Redox Biol. 2023;62:102663.
36. Ma JC, Luo T, Feng B, Huang Z, Zhang Y, Huang H, Yang X, Wen J, Bai X, Cui ZK. Exploring the translational potential of PLGA nanoparticles for intra-articular rapamycin delivery in osteoarthritis therapy. J Nanobiotechnol. 2023;21:361.
37. Cao H, Li W, Zhang H, Hong L, Feng X, Gao X, Li H, Lv N, Liu M. Bio-nanoparticles loaded with synovial-derived exosomes ameliorate osteoarthritis progression by modifying the oxidative microenvironment. J Nanobiotechnol. 2024;22:271.
38. Liu S, Zhang C, Zhou Y, Zhang F, Duan X, Liu Y, Zhao X, Liu J, Shuai X, Wang J, Cao Z. MRI-visible mesoporous polydopamine nanoparticles with enhanced antioxidant capacity for osteoarthritis therapy. Biomaterials. 2023;295:122030.
39. Zhan M, Sun H, Wang Z, Li G, Yang R, Mignani S, Majoral JP, Shen M, Shi X. Nanoparticle-mediated multiple modulation of bone microenvironment to tackle osteoarthritis. ACS Nano. 2024;18:10625–41.
40. Liu H, Wu X, Liu R, Wang W, Zhang D, Jiang Q. Cartilage-on-a-chip with magneto-mechanical transformation for osteoarthritis recruitment. Bioact Mater. 2024;33:61–8.
41. Wang P, Qian L, Liang H, Huang J, Jin J, Xie C, Xue B, Lai J, Zhang Y, Jiang L, et al. A polyvinyl alcohol/acrylamide hydrogel with enhanced mechanical properties promotes full-thickness skin defect healing by regulating immunomodulation and angiogenesis through paracrine secretion. Engineering. 2024.
42. Duan WL, Zhang LN, Bohara R, Martin-Saldaña S, Yang F, Zhao YY, Xie Y, Bu YZ, Pandit A. Adhesive hydrogels in osteoarthritis: from design to application. Mil Med Res. 2023;10:4.
43. Yang KC, Yang YT, Wu CC, Hsiao JK, Huang CY, Chen IH, Wang CC. Bioinspired collagen-gelatin-hyaluronic acid-chondroitin sulfate tetracopolymer scaffold biomimicking native cartilage extracellular matrix facilitates chondrogenesis of human synovium-derived stem cells. Int J Biol Macromol. 2023;240:124400.
44. Downs FG, Lunn DJ, Booth MJ, Sauer JB, Ramsay WJ, Klemperer RG, Hawker CJ, Bayley H. Multi-responsive hydrogel structures from patterned droplet networks. Nat Chem. 2020;12:363–71.
45. Feng Y, Zhang Z, Tang W, Dai Y. Gel/hydrogel-based in situ biomaterial platforms for cancer postoperative treatment and recovery. Exploration. 2023;3:20220173.
46. Zhang W, Zha K, Hu W, Xiong Y, Knoedler S, Obed D, Panayi AC, Lin Z, Cao F, Mi B, Liu G. Multifunctional hydrogels: advanced therapeutic tools for osteochondral regeneration. Biomater Res. 2023;27:76.
47. Riahi K, Dirba I, Ablets Y, Filatova A, Sultana SN, Adabifiroozjaei E, Molina-Luna L, Nuber UA, Gutfleisch O. Surfactant-driven optimization of iron-based nanoparticle synthesis: a study on magnetic hyperthermia and endothelial cell uptake. Nanoscale Adv. 2023;5:5859–69.
48. Kralchevsky PA, Danov KD, Petkov PV. Soft electrostatic repulsion in particle monolayers at liquid interfaces: surface pressure and effect of aggregation. Philos Trans A Math Phys Eng Sci. 2016;374.
49. Jiang Y, Hao M, Jiang F, Li J, Yang K, Li C, Ma L, Liu S, Kou X, Shi S, et al. Lyophilized apoptotic vesicle-encapsulated adhesive hydrogel sponge as a rapid hemostat for traumatic hemorrhage in coagulopathy. J Nanobiotechnol. 2023;21:407.
50. Huang C, Ye Q, Dong J, Li L, Wang M, Zhang Y, Zhang Y, Wang X, Wang P, Jiang Q. Biofabrication of natural Au/bacterial cellulose hydrogel for bone tissue regeneration via in-situ fermentation. Smart Mater Med. 2023;4:1–14.
51. Huang YF, Wang G, Ding L, Bai ZR, Leng Y, Tian JW, Zhang JZ, Li YQ, Ahmad, Qin YH, et al. Lactate-upregulated NADPH-dependent NOX4 expression via HCAR1/PI3K pathway contributes to ROS-induced osteoarthritis chondrocyte damage. Redox Biol. 2023;67:102867.
52. Liu L, Xian Y, Wang W, Huang L, Fan J, Ma W, Li Y, Liu H, Yu JK, Wu D. Meniscus-inspired self-lubricating and friction-responsive hydrogels for protecting articular cartilage and improving exercise. ACS Nano. 2023;17:24308–19.
53. Wang Y, Zhang S, Benoit DSW. Degradable poly(ethylene glycol) (PEG)-based hydrogels for spatiotemporal control of siRNA/nanoparticle delivery. J Control Release. 2018;287:58–66.


## Publisher's Note